A silent Kv channel subunit shapes PV neuron action potential waveform and short-term synaptic plasticity during high-frequency firing

Sanika Ganesh[1], Theresa M. Canty[1], Bernardo L. Sabatini[1*]

[1] Howard Hughes Medical Institute, Department of Neurobiology, Harvard Medical School, Boston, MA 02115, USA.

* Bernardo L. Sabatini
Email: bsabatini@hms.harvard.edu

Author Contributions: S.G. and B.L.S. designed research; S.G. and T.C. performed research; S.G., T.C., and B.L.S. analyzed data; S.G. and B.L.S. wrote the paper.

Competing Interest Statement: The authors declare no competing interests.

Classification: Biological Sciences, Neuroscience

Keywords: PV neuron, potassium channel, silent subunit, GABAergic, inhibition

This PDF file includes:

Main Text
Figures 1 to 5

Abstract

Fast-spiking parvalbumin-positive (PV) neurons provide precisely timed, context-dependent inhibition within cortical circuits. PV neuron firing properties are specialized among cortical neurons, suggesting that they express a unique complement of ion channels. Here, we identify the PV-specific silent voltage-gated potassium (Kv) channel subunit Kv6.4 (encoded by *Kcng4*), whose role in cortical PV neuron physiology was previously unknown, as a modulator of both intrinsic and synaptic properties. Kv6.4 does not form functional channels on its own but, as shown in prior work, assembles with Kv2 subunits to create heterotetrameric channel complexes, effectively reducing Kv2-mediated delayed rectifier current. We find that *Kcng4* expression is enriched within a distinct *Pvalb*-expressing subclass in primary somatosensory (S1) and motor (M1) cortex and emerges during postnatal development. In PV neurons, Kv6.4 loss reduces action potential (AP) height and width, hyperpolarizes the threshold and interspike potential, and accelerates AP upstroke particularly during repetitive firing. Kv6.4 loss, potentially due to the changes in AP waveform, also alters GABA release and paired-pulse depression at synapses made by PV onto pyramidal (PYR) neurons. The effects of Kv6.4 loss are amplified during high-frequency firing, within the physiological range of fast-spiking PV neurons, likely due to altered repolarization dynamics that accumulate across successive APs. These findings are thus consistent with the function of Kv6.4 in modifying Kv2-mediated delayed rectifier currents. Hence, Kv6.4 tunes the temporal precision of PV inhibitory output, a feature that may be critical for stable excitation-inhibition ratios and adaptive circuit function underlying learning and behavior.

Significance Statement

Voltage-gated ion channels are broadly expressed yet serve cell-type-specific functions. We demonstrate that the Kv6.4 silent subunit is selectively expressed by fast-spiking parvalbumin-positive (PV) inhibitory neurons among cortical neurons. In PV neurons, Kv6.4 modulates action potential (AP) waveform and GABA release onto excitatory neurons in a frequency-dependent

manner, well within the physiological range of PV firing. This mechanism is likely important for preserving the temporal precision of inhibition, which is particularly critical for fast-spiking interneuron output. By shaping short-term synaptic plasticity during high-frequency firing, Kv6.4 provides a molecular and cell-type-specific mechanism for context-dependent tuning of inhibition within cortical circuits. This function may be especially relevant for sensory processing, experience-dependent plasticity, and the maintenance of excitation-inhibition ratios *in vivo*.

Main Text

Introduction

The specific combination of ion channels expressed by each neuron shapes its physiological properties. Large-scale transcriptional analyses have systematically mapped and characterized the molecular signatures of many neuronal classes (1–10), yielding new insights into the variability of ion channel composition across cell classes. These transcriptional data can be integrated with electrophysiological analyses to reveal the mechanisms that govern the intrinsic excitability and synaptic properties of distinct neuron types.

In many brain areas, fast-spiking (FS) interneurons have unique electrophysiological characteristics such as the ability to maintain high rates of action potential (AP) firing. In cerebral cortex, fast-spiking parvalbumin-positive (PV) interneurons deliver precisely timed, potent inhibition by targeting the somatodendritic domain of excitatory pyramidal (PYR) neurons (11). As the largest class of cortical GABAergic neurons, PV neurons preserve network stability by providing cortical gain control (12–14), regulate the temporal precision of PYR neuron firing (15, 16), and gate experience-dependent plasticity (17, 18), especially during critical periods of cortical development (19). Disruptions in PV-cell-mediated inhibition have been implicated in neurological disorders such as epilepsy, schizophrenia, depression, autism spectrum disorder, and Alzheimer's disease (11, 20).

The diverse functions of PV neurons depend on their capacity for rapid, non-adapting AP firing. Particularly important to sustaining high AP firing rates are potassium (Kv) channels: Kv3 channels support the FS phenotype by facilitating rapid AP repolarization (21–23), whereas Kv1 channels regulate near-threshold excitability by setting AP threshold and first spike latency (24–26). In contrast, the physiological consequences of modulatory potassium channel subunits—nonconducting on their own, but capable of powerfully shaping the behavior of channel complexes—remain largely unexplored (27). These "silent" subunits represent a potentially critical yet understudied mechanism for tuning cellular excitability and circuit dynamics. Notably, their expression is more restricted than that of electrically active channels (28), raising the possibility that their cell-type-specific expression patterns may underlie the functional diversity of neuronal classes.

Multiple single-cell transcriptomic datasets indicate that across cerebral cortical neurons, *Kcng4*, a gene that encodes the nonconducting subunit Kv6.4, is selectively expressed in PV interneurons (3, 10). Prior analyses of cultured and peripheral neurons have demonstrated that Kv6.4 co-assembles with Kv2.1 to generate functional Kv2.1/Kv6.4 channels (29–36). These heterotetrameric channels exhibit a ~30–40 mV hyperpolarized shift in their voltage dependence of inactivation compared to Kv2.1 homomers, which effectively decreases Kv2 current (29, 30, 32–35). However, given the complex interactions between voltage-sensitive conductances, the impact of Kv6.4 expression on neuronal function is difficult to infer from the biophysical effects of Kv6.4 on Kv2.1 described in heterologous expression systems.

Here, we examine the expression of the Kv6.4 channel subunit in cortical neurons and its contribution to the physiology of cortical PV interneurons. We show that *Kcng4* expression is enriched within *Pvalb*-expressing neurons in primary somatosensory (S1) and motor (M1) cortex.

The timing of *Kcng4* expression during postnatal development, together with its spatial distribution, suggest a role in the physiology of mature FS neurons. To examine the function of Kv6.4, we used the Kcng4^{Cre} knock-in mouse line in which Cre recombinase replaces endogenous *Kcng4*, effectively knocking-out the gene. Whole-cell recordings show that Kv6.4 expression modifies AP shape and interspike potentials during repetitive firing without altering AP frequency. At the synaptic level, paired recordings show that a lack of Kv6.4 expression regulates PV inhibition onto nearby PYR neurons during fast spiking, thereby affecting short-term plasticity during rapid firing.

Results

Cortical PV neurons selectively express *Kcng4*

The potassium channel Kv6.4 subunit, encoded by *Kcng4*, forms heterotetrameric channels with Kv2.1, encoded by *Kcnb1*. To characterize the expression of these potassium channel subunits in cortical PV neurons, we performed multiplexed fluorescent *in situ* hybridization (FISH) to examine the expression of *Kcng4*, *Kcnb1*, and *Pvalb* (n = 6 mice with 18 sections and 36 hemispheres per region, 2–4 sections per mouse) in M1 and S1 in wildtype C57BL/6J mice (**Fig. 1 *A*–*B***).

We detected expression of *Kcng4* across cortical layers in M1 and S1, roughly mirroring that of *Pvalb* (**Fig. 1 *C*–*D***). High-resolution images demonstrate *Kcng4* and *Pvalb* co-expression within individual cells (**Fig. 1*C***). Indeed, nearly all *Kcng4*+ cells express *Pvalb* (M1: 0.88 ± 0.025, S1: 0.95 ± 0.009), and a substantial proportion of *Pvalb*+ neurons express *Kcng4* (M1: 0.25 ± 0.014, S1: 0.39 ± 0.020), with higher co-expression of *Pvalb* and *Kcng4* in S1 compared to M1 (**Fig. 1*E*** and **Dataset S1**). These cortical co-expression patterns are reminiscent of those observed in PV neurons of the external globus pallidus (GPe), where ~90% of *Kcng4*+ neurons express *Pvalb*, and ~30% of *Pvalb*+ neurons express *Kcng4* (37). In both M1 and S1, co-expression patterns were consistent across layers (L; **Fig. 1*D***). However, we noted high enrichment of *Kcng4* in S1 L4 *Pvalb*+ neurons (S1 L4: 0.70 ± 0.027; **Fig. 1*E*** and **Dataset S1**). We found that almost every neuron that co-expressed *Kcng4* and *Pvalb* also expressed *Kcnb1* (*Kcnb1*: 0.99 ± 0.003; **Dataset S1**). While most functional studies of Kv6.4 have reported its assembly with Kv2.1 (29–35, 38), Kv2.1 and Kv2.2 (encoded by *Kcnb2*) can be expressed independently (39) and interact with Kv6.4 (36). Both *Kcnb1* and *Kcnb2* are expressed by PV neurons (**Fig. S1*C***).

The results of these FISH analyses are consistent with spatial transcriptomic data from the Allen Brain Cell (ABC) Atlas (10), which confirm that *Kcng4* is selectively expressed in *Pvalb*+ neurons in M1 and S1 (**Fig. S1*A***). We also noted that *Kcng4*+ neurons comprise a unique transcriptionally defined supertype (supertype 207) of *Pvalb*+ interneurons (**Fig. S1*B***), as defined by the ABC Atlas (10).

Spatiotemporal patterns of Kcng4^{Cre} activation

Pvalb expression emerges around postnatal day (P) 12, and PV neuron maturation restricts critical periods of heightened sensory-motor cortical plasticity (18, 19, 25, 40). Therefore, we examined the onset of Kv6.4 expression. We generated Kcng4^{Cre}; Ai14 mice by crossing a transgenic mouse line in which Cre is knocked into the *Kcng4* locus (Kcng4^{Cre}), resulting in a functional knock-out, to a reporter line that expresses tdTomato in a Cre-dependent manner (Ai14). We used tdTomato fluorescence to compare Kcng4^{Cre} activation in M1 and S1 of young (2 weeks) and adult (5+ weeks) heterozygous (Kcng4$^{Cre/WT}$; Ai14) and homozygous (Kcng4$^{Cre/Cre}$; Ai14) mice (**Fig. 2*A***). Because Cre replaces the endogenous *Kcng4* coding sequence in Kcng4^{Cre} mice, heterozygous mice retain one functional *Kcng4* allele, and homozygous mice lack functional *Kcng4* alleles entirely. We therefore expected Cre-driven tdTomato expression to exhibit a gene-dosage effect, with higher Cre reporter activation in homozygous than heterozygous mice. Consistent with this expectation, tdTomato fluorescence was modestly higher

in homozygous mice (**Fig. 2 *B–D*).** Importantly, both genotypes showed weak labeling in young mice and strong labeling in adult mice in M1 and S1 (**Fig. 2 *B–D*).** High-resolution imaging at the 2-week timepoint revealed that tdTomato-labeled cortical cells in young animals exhibit astrocytic morphology, characterized by extensive arborization and a lack of polarized processes (**Fig. S2 *A–C***). These results suggest that there is minimal Kcng4^{Cre} activation in PV neurons at early developmental stages, and that Kv6.4 expression arises after maturation of PV neurons, specifically in M1 and S1.

In adult mice, Kcng4^{Cre}-mediated expression of tdTomato occurs in brain regions that contain fast-spiking neurons, such as the cerebral cortex, GPe, and cerebellum (**Fig. S3**). Indeed, *Kcng4*+ neurons have previously been identified as a subclass of PV neurons in the GPe (37). In the cerebellum, *Kcng4* expression is enriched in fast-spiking Purkinje cells (**Fig. S1*D***) as may be expected from our observations, given that PV neurons include some but not all Purkinje cells (6). The spatial distribution of tdTomato+ neurons is thus consistent with Kv6.4 expression in fast-spiking neuronal populations across multiple brain regions. Together, the spatial and temporal patterns of Kcng4^{Cre} activation raise the possibility that Kv6.4 shapes the fast-spiking phenotype of PV neurons.

Kv6.4 modulates AP height, AP half-width, and interspike potential in PV neurons

Given that Kv6.4 reduces delayed rectifier Kv2-mediated current in heterologous expression systems (29, 30, 32–35), the removal of Kv6.4 in PV neurons is expected to increase net Kv2 current. This could have widespread effects on the intrinsic properties of PV neurons, such as AP shape and interspike potential. Thus, to study the impact of Kv6.4 on PV neuron physiology, we performed whole-cell current-clamp recordings in fast-spiking neurons from L2/3 wildtype *Kcng4* (n = 18 cells in 4 mice, PV$^{Cre/WT}$; Ai14), heterozygous *Kcng4* knock-out (n = 16 cells in 4 mice, Kcng4$^{Cre/WT}$; Ai14), and homozygous *Kcng4* knock-out (n = 20 cells in 4 mice, Kcng4$^{Cre/Cre}$; Ai14) mice carrying two (WT/WT), one (Cre/WT), or no (Cre/Cre) copies of *Kcng4*, respectively. In each genotype, recordings were made from tdTomato-expressing neurons in age-matched adult animals. Because S1 *Pvalb*+ neurons are more likely to express *Kcng4* than M1 *Pvalb*+ neurons (**Fig. 1*E***), we conducted electrophysiological recordings in S1. We used a series of current injections to measure voltage (–200 to 200 pA, 40 pA increments) and AP (200 to 1200 pA, 100 pA increments) responses across all three genotypes, blinded to heterozygous and homozygous animals from which acute brain slices were prepared (**Fig. 3*A***). We used littermates to compare heterozygous and homozygous animals. Although we observed no significant gross differences in current–voltage or current–firing rate relationships across genotypes (**Fig. 3*B*** and **Dataset S2**), we observed several significant differences in intrinsic properties between wildtype, heterozygous, and homozygous mice, in line with our expectation that Kv6.4 loss alters Kv2-mediated delayed rectifier current.

Indeed, AP height, AP half-width, and interspike potential differed significantly between groups (**Fig. 3 *C–F*** and **Dataset S2*)***. To standardize analysis across cells with varying rheobase, we analyzed the first trace containing at least 10 APs and restricted analysis to the 2nd and 10th APs in these traces to survey early and later phases of the AP train. AP height was lower in homozygous mice compared to wildtype for the 2nd AP (WT/WT = 85.05 ± 1.00 mV, Cre/WT = 82.84 ± 1.10 mV, Cre/Cre = 81.44 ± 0.95 mV; one-way ANOVA, p = 0.041; Tukey–Kramer post hoc comparisons: WT/WT vs Cre/WT p = 0.297, WT/WT vs Cre/Cre p = 0.032, Cre/WT vs Cre/Cre p = 0.597), and for the 10th AP (**Fig. 3 *C–D*** and **Dataset S2**). Half-width was also significantly reduced in homozygous mice, both for the 2nd AP (WT/WT = 0.22 ± 0.01 ms, Cre/WT = 0.23 ± 0.01 ms, Cre/Cre = 0.20 ± 0.01 ms; one-way ANOVA, p = 0.007; Tukey–Kramer post hoc comparisons: WT/WT vs Cre/WT p = 0.911, WT/WT vs Cre/Cre p = 0.030, Cre/WT vs Cre/Cre p = 0.013) and the 10th AP (**Fig. 3 *E–F*** and **Dataset S2**). Additionally, the interspike potential, defined as the most negative potential between APs, was more negative in homozygous mice for the 2nd AP (WT/WT = –69.55 ± 0.86 mV, Cre/WT = –68.81 ± 0.83 mV,

Cre/Cre = –71.87 ± 0.72 mV; one-way ANOVA, p = 0.022; Tukey–Kramer post hoc comparisons: WT/WT vs Cre/WT p = 0.805, WT/WT vs Cre/Cre p = 0.098, Cre/WT vs Cre/Cre p = 0.026) and the 10th AP (**Fig. 3 *G–H*** and **Dataset S2**). Bootstrapping analysis further confirmed differences in the distributions across groups (**Fig. 3 *C, E,* and *G***). These results indicate that Kv6.4 loss decreases AP amplitude and duration and deepens the interspike potential in PV neurons. These effects are consistent with the known mechanism through which Kv6.4 reduces Kv2 current, namely by shifting heterotetramer inactivation to more negative potentials.

Additionally, we examined AP threshold, AP maximum slope, afterhyperpolarization (AHP) amplitude for a train of APs, and sag voltage across the three groups. We found that the three groups differed significantly in AP threshold for the 10th AP (WT/WT = –42.14 ± 0.81 mV, Cre/WT = –42.00 ± 0.58 mV, Cre/Cre = –44.14 ± 0.60 mV; one-way ANOVA, p = 0.046; Tukey–Kramer post hoc comparisons: WT/WT vs Cre/WT p = 0.988, WT/WT vs Cre/Cre p = 0.090, Cre/WT vs Cre/Cre p = 0.076), but not for the 2nd AP (**Fig. S4 *A–B*** and **Dataset S2**), suggesting that Kv6.4 loss contributes to maintaining a lower AP threshold particularly over the course of repetitive firing (**Fig. S4*B***). AP maximum slope was also significantly higher at the 10th AP in homozygous mice (WT/WT = 452.02 ± 11.98 V/s, Cre/WT = 432.02 ± 22.33 V/s, Cre/Cre = 488.23 ± 13.40 V/s; one-way ANOVA, p = 0.047; Tukey–Kramer post hoc comparisons: WT/WT vs Cre/WT p = 0.666, WT/WT vs Cre/Cre p = 0.233, Cre/WT vs Cre/Cre p = 0.042), but no differences were observed at the 2nd AP (**Fig. S4 *C–D*** and **Dataset S2**). Thus, when Kv6.4 is absent, fast-spiking neurons exhibit an increased upstroke velocity during repetitive firing. There were no significant differences in the AHP amplitude (**Fig. S4 *E–F*** and **Dataset S2**) or sag voltage (**Fig. S4 *G–H*** and **Dataset S2**), which is consistent with the limited role of Kv6.4 in the conductances underlying these parameters. As discussed previously, Kv6.4 loss is predicted to increase net Kv2-mediated repolarizing drive, and consistent with this prediction, the interspike potential is hyperpolarized in PV neurons that do not express *Kcng4* (**Fig. 3 *G-H*** and **Dataset S2**). This deeper hyperpolarization is expected to enhance the recovery of voltage-gated sodium (Nav) channels from inactivation during repetitive firing (41). Thus, in the absence of Kv6.4, enhanced Nav channel availability likely contributes to the more hyperpolarized AP threshold and faster AP upstroke velocity that we observe during sustained firing in PV neurons.

To determine whether the differences between groups generalize across firing rates, we analyzed AP height, half-width, interspike potential, threshold potential, and maximum slope across all recordings, with data organized into bins containing comparable numbers of APs (**Fig. S5*A***). We found that differences in genotype persist across firing rates (**Fig. S5 *B–F***), indicating that these effects are not limited to a single firing rate regime. Thus, group differences in these metrics are robust to the trace selection criterion described previously (2nd and 10th AP within the first trace containing ≥10 APs for the analysis shown in **Fig. 3** and **Fig. S4**). The shorter AP duration in homozygous animals is not attributable to adaptation of the interspike interval (ISI; ms), as the groups exhibit a similar change (Δ) in ISI between early and late spikes ($ISI_{49\text{-}50} – ISI_{2\text{-}3}$) in recordings containing ≥50 APs (**Fig. S5*G***). Notably, homozygous animals display attenuated within-trace adaptation in AP half-width and interspike potential between early and late spikes ($AP_{50} – AP_2$; **Fig. S5 *H–I***). This reduced adaptation in AP half-width becomes more pronounced at higher firing rates (**Fig. S5*H***). Hence, Kv6.4 loss deepens the interspike potential and shortens action potentials across all firing rates examined, with increasing effects at higher firing frequencies.

Because the S1 L2/3 WT PV population includes both *Kcng4*-expressing and non-expressing neurons, differences between wildtype, heterozygous, and homozygous animals may reflect differences in PV neuron subtypes, rather than specific physiological effects of removing the Kv6.4 silent subunit. Specifically, roughly 35% of S1 L2/3 PV neurons express *Kcng4*. However, phenotypes that differ between the heterozygous and homozygous mice isolate effects within neurons that typically express *Kcng4*. These include AP half-width, interspike potential, and AP maximum slope, indicating that these alterations in AP waveform reflect Kv6.4 loss rather than

263 variability between PV subclasses or differences in mouse genetic background. In contrast,
264 differences in AP height and AP threshold may be influenced by the inclusion of *Kcng4* non-
265 expressing neurons in the WT group. Nonetheless, these effects are consistent with the expected
266 mechanisms through which Kv6.4 loss modifies Kv2 repolarization and associated Nav
267 availability, suggesting that these effects arise from physiological changes rather than PV neuron
268 subtype variability.
269
270 Hence, especially during repetitive firing, Kv6.4 deletion yields more negative interspike and
271 threshold potentials, faster AP upstrokes, and narrower and smaller APs. These altered intrinsic
272 properties are consistent with the expected increase in Kv2 repolarizing current and enhanced
273 recovery of Nav current. Notably, these alterations do not result in a higher firing frequency but
274 rather appear to refine the response of PV neurons during periods of high activity. Therefore,
275 Kv6.4 shapes the AP waveform in PV neurons, particularly during high-frequency firing.
276
277 **Kv6.4 regulates paired-pulse depression at PV–PYR synapses during high-frequency AP**
278 **firing**
279
280 Motivated by the possibility that Kv6.4-dependent changes in PV action potential waveform could
281 alter GABA release, we next investigated inhibitory transmission at PV–PYR synapses. To study
282 the consequences of Kv6.4 ablation on inhibitory synapses, we performed paired whole-cell
283 recordings in L2/3 PV neurons and connected PYR neurons (**Fig. 4*A***). This analysis included
284 wildtype (n = 11 pairs in 9 mice) and homozygous (n = 10 pairs in 8 mice) groups. We evoked
285 action potentials in PV neurons by current injection under current-clamp and simultaneously
286 measured the resulting inhibitory postsynaptic currents (IPSCs) in neighboring PYR neurons
287 under voltage-clamp (**Fig. 4*B***). Excitatory currents were pharmacologically blocked. PYR neuron
288 recordings used a high-chloride cesium-based internal solution to amplify inhibitory currents,
289 resulting in inward GABAergic currents at resting membrane potentials. Synaptic currents were
290 also converted to conductance to isolate postsynaptic channel activation independent of
291 recording conditions (see ***Synaptic Properties*** in ***Materials and Methods***). We did not identify
292 differences in IPSC peak amplitude, whether assessed as current or conductance, or in the
293 passive properties (membrane resistance, membrane capacitance, or membrane time constant)
294 of PYR neurons between groups (**Fig. 4*C*** and **Dataset S3**).
295
296 We found that Kv6.4 modulates synaptic depression during high-frequency firing, as indicated by
297 altered inhibitory currents in response to paired-pulse stimulation. Specifically, we recorded
298 IPSCs in PYR neurons triggered by pairs of action potentials in PV neurons with varying
299 interstimulus intervals (Δt = 10, 20, 50, 100, 200, 500, 1000 ms; **Fig. 4*D***). The amplitude of
300 overlapping IPSCs was quantified by subtracting the residual decay of the first IPSC from the
301 peak of the second (see ***Synaptic Properties*** in ***Materials and Methods***). We observed that the
302 paired-pulse ratio of inhibition (PPR_i) and conductance (PPR_g) is significantly higher in mice that
303 lack Kv6.4 compared to control mice, but only at short interstimulus intervals, Δt = 10 ms (PPR_i:
304 WT/WT = 0.52 ± 0.031, Cre/Cre = 0.68 ± 0.035; unpaired two-tailed t-test, p = 0.003; PPR_g:
305 WT/WT = 0.52 ± 0.036, Cre/Cre = 0.69 ± 0.038; unpaired two-tailed t-test, p = 0.005) and Δt = 20
306 ms (PPR_i: WT/WT = 0.50 ± 0.036, Cre/Cre = 0.60 ± 0.016; unpaired two-tailed t-test, p = 0.022;
307 PPR_g: WT/WT = 0.48 ± 0.035, Cre/Cre = 0.57 ± 0.020; unpaired two-tailed t-test, p = 0.043) (**Fig.**
308 **4*E*** and **Dataset S3**). This indicates that removal of Kv6.4 alters presynaptic GABA release
309 properties of PV neurons. The observed differences are consistent with a reduction in probability
310 of GABA release per release site in mice lacking *Kcng4*, although paired-pulse measurements
311 alone cannot distinguish reduced release probability from alternative and not mutually exclusive
312 mechanisms such as enhanced short-term facilitation. In either case, differences in presynaptic
313 properties between groups, such as Ca^{2+} entry triggering neurotransmitter release, can be
314 explained by the altered spike waveform observed in knockout neurons (**Fig. 3**, **Fig. S5**).
315 Moreover, the relationship between paired-pulse ratio and interstimulus interval was significantly
316 different between genotypes (repeated-measures ANOVA; current, p = 0.032; conductance, p =

0.038; **Dataset S3**), indicating that synaptic depression varied across interstimulus intervals as a function of Kv6.4 expression. Thus, paired-pulse depression is reduced at PV–PYR synapses in the absence of Kv6.4 expression for presynaptic APs firing faster than ~50 Hz, which is well below the maximal firing rates (hundreds of Hz) of cortical PV neurons *in vivo* (42).

We observed similar trends in the amplitude of inhibitory currents elicited by a 5-pulse train, normalized to the first pulse: effects were only apparent at the shortest interstimulus interval (**Fig. 4 *F–H*** and **Dataset S3**). As the decay of preceding IPSCs was not corrected in the analysis of 5-pulse train measurements (see ***Synaptic Properties*** in ***Materials and Methods***), the differences between groups in this analysis may appear less pronounced than in the paired-pulse analysis. At Δt = 10 ms, both current (WT/WT = 0.65 ± 0.025, Cre/Cre = 0.78 ± 0.051; unpaired two-tailed t-test, p = 0.022) and conductance (WT/WT = 0.61 ± 0.027, Cre/Cre = 0.76 ± 0.059; unpaired two-tailed t-test, p = 0.035) were significantly higher for the third pulse in homozygous mice. No differences were detected for other pulses or interstimulus intervals in individual comparisons, and repeated-measures ANOVA across all five pulses revealed no significant overall effect of genotype, although a trend toward higher normalized amplitudes in the absence of Kv6.4 was observed at the shortest interstimulus interval (**Fig. 4 *G–H***, **Fig. S*6***, and **Dataset S3**).

As with many knockout-based approaches, interpretation of genotype-dependent effects must acknowledge that the targeted gene is not uniformly expressed across all neurons of the targeted cell type. As discussed previously, WT recordings therefore include a mix of *Kcng4*-expressing and non-expressing neurons and may sample from different PV subpopulations. Nevertheless, the differences in repolarization observed between heterozygous and homozygous neurons (**Fig. 3**, **Fig. S5**), both of which normally express *Kcng4* and therefore control for PV subtype diversity, offer a plausible mechanistic basis for the synaptic phenotype. Specifically, the shortening of action potentials caused by Kv6.4 loss is expected to alter presynaptic calcium entry in ways that could influence GABA release.

Together, these results demonstrate that Kv6.4 selectively tunes synaptic depression at PV–PYR synapses during high-frequency activity, without influencing steady-state inhibition or IPSCs at longer interstimulus intervals. These data reveal a function for Kv6.4 in regulating the precision of inhibitory signaling at cortical PV–PYR synapses under fast-spiking conditions.

Discussion

Our findings reveal that Kv6.4 expression shapes both the intrinsic properties and synaptic output of PV neurons during high-frequency firing (**Fig. 5**). Altered repolarization dynamics likely emerge at the interspike potential and accumulate during repetitive firing, progressively modifying the AP waveform, reducing its duration, amplitude, and threshold while increasing upstroke velocity. These waveform changes likely modify synaptic release during high-frequency firing, consistent with our observation of altered paired-pulse ratios at short interstimulus intervals. Thus, Kv6.4 regulates PV inhibition onto pyramidal neurons in a frequency-dependent manner.

The effects of Kv6.4 are likely mediated through its interactions with Kv2 subunits. The altered interspike potential observed in Kv6.4 knock-out neurons is consistent with prior findings that Kv6.4 subunits influence the inactivation properties of Kv2 heterotetramers (29, 30, 32–35). Kv2 current provides repolarizing drive that accumulates during high-frequency trains due to its slow kinetics, preventing AP broadening (28, 43–45). Loss of Kv2.1 prolongs APs and broadens Ca^{2+} transients specifically during high-frequency firing (43). In line with this, Kv6.4 likely broadens APs in PV neurons by reducing Kv2 current density, as it promotes the inactivation of its Kv2 partners during repolarization (29, 30). The contribution of Kv6.4 likely accompanies secondary effects to other potassium and sodium channels that further influence the spike train (41).

Kv6.4 depolarizes the interspike potential and broadens the AP waveform in PV neurons, which we propose may subsequently elevate the initial probability of GABA release at PV–PYR cell synapses, resulting in the enhanced paired-pulse depression observed (**Fig. 5**). Subtle alterations in AP waveform, and consequently in presynaptic Ca^{2+} entry, are known to exert supralinear effects on postsynaptic current amplitude (46–48), underscoring the sensitivity of neurotransmitter release to AP narrowing or broadening. In PV neurons, Ca^{2+} channels and GABA release are tightly coupled to rapidly translate changes in AP waveform into graded inhibition (11). Deletion of both *Kcng4* alleles results in a ~10% change in AP width (**Fig. 3** and **Dataset S2**) but a ~30% change in paired-pulse ratio (**Fig. 4** and **Dataset S3**). This ~3-fold amplification of Kv6.4-dependent effects is expected if AP broadening is also present in the presynaptic boutons of PV neurons. Kv3 channels have long been recognized as the primary regulators of rapid firing in PV neurons and synaptic depression at PV–PYR synapses through AP narrowing (22, 49). We demonstrate that a silent ion channel subunit engages these dynamics to modulate PV inhibition in a firing-frequency-dependent manner, a mechanism that is particularly relevant to fast-spiking interneurons.

The observed increase in paired-pulse ratios in *Kcng4*-knockout neurons is consistent with a reduction in release probability per release site. The loss of Kv6.4 shortens spike duration measured at the soma (**Fig. 3**, **Fig. S5**). If this effect is also present in the axon, it likely modifies presynaptic Ca^{2+} entry by decreasing the number of voltage-gated calcium channels opened per AP, thus altering both release probability and paired-pulse ratios. However, the peak amplitude of IPSCs in PYR neurons evoked by a single AP in a neighboring PV neuron was unaffected by loss of Kv6.4, suggesting potential compensatory changes in the number of release sites or postsynaptic GABA receptors per PV input. Nevertheless, our results do not establish the mechanisms by which Kv6.4 alters synaptic transmission between PV and PYR neurons. Additional direct or compensatory effects of Kv6.4 loss on Ca^{2+} entry, Ca^{2+} handling, or the release apparatus may also contribute. Future experiments directly measuring presynaptic Ca^{2+} entry can help discriminate between these mechanisms.

Kv6.4 is expected to share Kv2 subcellular localization patterns, forming clusters at the somatodendritic membrane (43, 44). The recent availability of effective Kv6.4 antibodies (36) will enable direct assessment of its localization in PV neurons. The broader expression pattern of Kv2.1 supports regulation of excitability across cell types, whereas the selective enrichment of Kv6.4 in PV neurons enables precise, cell-type-specific control of inhibitory output during high-frequency firing.

***Kcng4*+ as a functional PV subclass in cortical development and plasticity**

We find that the Kv6.4 silent subunit is selectively enriched in mature PV neurons—with minimal expression in other cortical cell types aside from astrocytes—and is restricted to a distinct transcriptional supertype of PV neurons (10). This specificity distinguishes Kv6.4 from broadly expressed potassium channels, such as Kv2.1 or Kv3.1 (3), making it an attractive candidate for selective targeting of this PV subclass. *Kcng4* has been identified as a marker of a PV subclass in the GPe (37), where *Kcng4*+ neurons were implicated in motor pattern regulation, but their physiological properties had not been defined. Here, we link this molecularly defined PV supertype to distinct physiological properties. Recent efforts in the molecular targeting of inhibitory neuron types have advanced our ability to dissect and manipulate circuit function across species (50). Kv6.4 thus represents a molecular marker of a specialized PV subclass with previously uncharacterized physiological roles, offering a new axis for selective circuit interrogation and tool development.

Kv6.4 expression confers a frequency-dependent mechanism for modulating PV output, which may facilitate adaptive changes in cortical circuits given that PV neurons form dense, nonspecific wiring with PYR neurons (51). *Kcng4* expression broadly parallels the spatiotemporal pattern of

Pvalb but is particularly enriched in S1 L4, where sensory inputs first reach somatosensory cortex (52) and where inhibition mediates experience-dependent plasticity during critical periods (17, 52). The onset of Kv6.4 expression may also influence early sensory-driven plasticity (52). Indeed, PV-mediated experience-dependent plasticity in S1 is regulated by potassium channel function (18) and transcription (26). The role of Kv6.4 may be particularly relevant to motor and sensory learning, as we and others have found that Kv6.4 is enriched in mouse motor and sensory areas (36) and is involved in sensing pain (32, 34, 35). Thus, Kv6.4 could link short-term synaptic plasticity with long-term learning, and disruptions in its function could interfere with cortical excitation-inhibition, plasticity, and development.

Pathophysiological implications of Kv6.4 dysfunction

Cortical circuit dysfunction in developmental and neurodegenerative disorders often arises from dysregulation of ion channels and GABAergic inhibition. Several voltage-gated ion channels and their regulators have been implicated in autism spectrum disorder, epilepsy, intellectual disability, and Alzheimer's disease, such as the voltage-gated sodium channels Nav1.1 and Nav1.2 (50, 53), the synaptic adhesion molecule Cntnap4 (54), the Kv3 channel family (55), and NRG1-ErbB4 signaling that modulates Kv1.1 channels (25). These mechanisms operate within defined developmental windows or neuronal populations, such as PV neurons, to regulate excitability, plasticity, and network stability, and the disruption of these functions can result in abnormal sensory processing and cognitive deficits.

Kv6.4 has recently emerged as a clinically relevant modulator of neuronal excitability, motivating further investigation into its role in PV neurons *in vivo*. Loss-of-function *Kcng4* mutations in humans have been associated with reduced pain sensitivity in migraine (28, 34, 35) and labor during pregnancy (32), likely due to altered function of Kv2.1/Kv6.4 heterotetramers and disrupted excitability. Kv2.1/Kv6.4 complexes exhibit reduced sensitivity to channel blockers compared with Kv2.1 alone (33), and new pharmacological tools can distinguish silent Kv subunits from standard delayed rectifiers (56). These approaches can be leveraged to identify and target Kv6.4-containing complexes for functional or therapeutic studies. Complete Kv6.4 loss is poorly tolerated, as homozygous mutations are associated with male sterility (57) and hydrocephalus (58) in mice, suggesting that dosage-sensitive or cell-type-specific approaches may be necessary for potential interventions. Mutations in Kv2 channels resulting in complete or partial channel loss-of-function are linked to epilepsy and neurodevelopmental disorders such as autism spectrum disorder and intellectual disability, marked by seizures, motor and language problems, behavioral deficits, and ataxia (28, 59–62). Homozygous *Kcnb1* deletion in mice results in hippocampal hyperexcitability, epileptiform activity, accelerated seizure progression, locomotor hyperactivity, and impaired spatial learning (63). Future studies could examine how Kv6.4/Kv2.1 heterotetramers govern the timing and strength of PV-mediated inhibition during sensory processing and learning *in vivo*, and how these mechanisms are disrupted in disease.

Materials and Methods

Mice

We used Kcng4^{Cre} (The Jackson Laboratory, RRID:IMSR_JAX:029414) and PV^{Cre} (The Jackson Laboratory, RRID:IMSR_JAX:017320) mouse lines in this study. Both lines were crossed to the Ai14 reporter line (The Jackson Laboratory, RRID:IMSR_JAX:007914) to fluorescently label cells with tdTomato following Cre-mediated recombination. All Ai14 reporter animals (B6.Cg background) were heterozygous for the Ai14 allele. Kcng4^{Cre} (B6.129(SJL) background) is a knock-in/knock-out line in which Cre recombinase is inserted into exon 2 of the *Kcng4* gene, disrupting endogenous *Kcng4* gene expression. Kcng4^{Cre} animals used in this study were heterozygous (Kcng4$^{Cre/WT}$) or homozygous (Kcng4$^{Cre/Cre}$) for the Cre allele in addition to carrying one allele of Ai14. PV^{Cre} (B6.129P2 background) is a knock-in line in which Cre recombinase is

478 inserted downstream of the *Pvalb* gene, without disrupting endogenous *Pvalb* gene expression.
479 PV^{Cre} animals used in this study were heterozygous for the Cre allele ($PV^{Cre/WT}$) in addition to
480 carrying one allele of Ai14. These animals, which retain two copies of *Kcng4*, were used as
481 wildtype control mice with labelling of PV neurons for experiments that require PV neuron
482 identification (e.g. whole-cell patch-clamp recordings). Additionally, we used C57BL/6J mice (The
483 Jackson Laboratory, RRID:IMSR_JAX:000664) as wildtype control mice and for backcrossing.
484
485 We used mice between 2 and 20 weeks of age, with approximately balanced sex ratios. Mice
486 were maintained on a 12h light/dark cycle under standard housing conditions. All experiments
487 were performed in accordance with protocols approved by the Harvard Standing Committee on
488 Animal Care (Protocol #: IS00000571-6), following guidelines described in the US NIH Guide for
489 the Care and Use of Laboratory Animals.
490
491 **Fluorescent RNA in situ hybridization**
492
493 Wildtype mice (5–7 weeks old) were anesthetized with isoflurane, and brains were rapidly
494 extracted and embedded in freezing media (Tissue-Tek O.C.T. Compound) on dry ice. Fresh-
495 frozen brains were cryosectioned at 20 µm thickness (Leica CM3050S), adhered to SuperFrost
496 Plus glass slides (VWR), and immediately refrozen, with short-term sample storage at –20°C and
497 long-term sample storage at –80°C. Multiplexed fluorescent RNA in situ hybridization (FISH) was
498 performed using the RNAscope Reagent Kit v2 (Advanced Cell Diagnostics, ACD) in
499 collaboration with the Harvard Medical School Neurobiology Imaging Facility. The tissue was
500 processed according to manufacturer instructions using a Protease III treatment for 30 min at
501 room temperature. The following probes were used: Mm-*Pvalb* (ACD 421931), Mm-*Kcng4* (ACD
502 316931-C2), and Mm-*Kcnb1* (ACD 316941-C3). Samples were validated using positive and
503 negative control probes, and nuclei were counterstained with DAPI. Samples were then imaged
504 on an Olympus VS200 slide scanning microscope using a 20x objective and a Leica Stellaris 8
505 confocal microscope with a 63x oil-immersion objective. ROIs were drawn manually and
506 quantified using QuPath, with further analysis in MATLAB (R2024a).
507
508 **Histology**
509
510 Mice (2-20 weeks old) were anesthetized with isoflurane and transcardially perfused with 4%
511 paraformaldehyde (PFA) in phosphate-buffered saline (PBS). Brains were dissected and
512 postfixed in 4% PFA overnight at 4°C and transferred to 30% sucrose for at least 1 day prior to
513 cryosectioning. Brains were embedded in freezing media (Tissue-Tek O.C.T. Compound),
514 coronally sectioned at 50 µm thickness (Leica CM3050S), and stored in PBS at 4°C. Sections
515 were stained with DAPI (Sigma-Aldrich D9542) for 10 minutes at room temperature, mounted on
516 SuperFrost Plus glass slides (VWR), and coverslipped with mounting medium (ProLong™ Gold
517 Antifade Mountant). Samples were imaged on an Olympus VS200 slide scanning microscope
518 using a 20x objective and a Leica Stellaris 8 confocal microscope with a 63x oil-immersion
519 objective.
520
521 **Acute slice preparation**
522
523 Mice (5-7 weeks old) were anesthetized with isoflurane and immediately decapitated following
524 transcardial perfusion with ice-cold artificial cerebrospinal fluid (ACSF) containing (in mM): 125
525 NaCl, 2.5 KCl, 25 $NaHCO_3$, 2 $CaCl_2$, 1 $MgCl_2$, 1.25 NaH_2PO_4, and 17 glucose (300–310 mOsm
526 kg^{-1}). Extracted brains were transferred to a Leica VT1200s vibratome for preparation of 300 µm
527 coronal slices in ice-cold ACSF. After cutting, slices were incubated for 3–6 min in choline-based
528 solution at 34°C containing (in mM): 110 choline chloride, 25 $NaHCO_3$, 2.5 KCl, 7 $MgCl_2$, 0.5
529 $CaCl_2$, 1.25 NaH_2PO_4, 25 glucose, 11.6 ascorbic acid, and 3.1 pyruvic acid (320–330 mOsm
530 kg^{-1}). In a second chamber, slices were incubated in ACSF at 34°C for 1 h. The slices were then

cooled to room temperature (> 1h) and maintained until electrophysiology recordings were performed. All solutions were continuously bubbled with carbogen gas (95% O_2, 5% CO_2).

Whole-cell patch-clamp recordings were conducted in L2/3 of primary somatosensory cortex (S1) in artificial cerebrospinal fluid (ACSF) at 30–32°C with a perfusion rate of 4–6 mL min^{-1}. Layer 2/3 was defined as spanning from 100–200 µm to 400–500 µm below pia. tdTomato+ neurons were identified using a Scientifica microscope equipped with a digital camera (Hamamatsu), an epifluorescence LED light source (CoolLED), and a 60x/0.9NA LUMPlanFl/IR water-immersion objective (Olympus). Patch pipettes were pulled from borosilicate glass (Sutter Instruments) with resistances of 2.0–3.5 MΩ. Recordings were performed using a Multiclamp 700B amplifier (Molecular Devices) and a data acquisition board (National Instruments). Data were collected and analyzed using MATLAB custom-written software and scripts (R2023a).

Intrinsic properties

For whole-cell current-clamp recordings assessing intrinsic properties, patch pipettes were filled with low chloride potassium-based internal solution (in mM): 135 $KMeSO_3$, 3 KCl, 10 HEPES, 1 EGTA, 0.1 $CaCl_2$, 4 Mg-ATP, 0.3 Na-GTP, and 8 Na_2Phosphocreatine (pH 7.3 adjusted with KOH, 290–300 mOsm kg^{-1}). The following synaptic blockers were bath-applied: NBQX (10 µM, Tocris), CPP (10 µM, Tocris), and SR 95531 hydrobromide (10 µM, Tocris). Signals were filtered at 10 kHz and digitized at 50 kHz.

The experimenter was blinded to heterozygous (Kcng4$^{Cre/WT}$; Ai14) and homozygous (Kcng4$^{Cre/Cre}$; Ai14) genotypes, and age-matched littermates were used. Neuronal responses were measured to current steps delivered at both (1) the neuron's endogenous resting membrane potential and (2) at –70 mV maintained via continuous current injection. Resting membrane potential was measured shortly after breaking in, after which all other intrinsic properties were measured. Action potential threshold was defined as the membrane potential at which the dV/dt exceeded 4% of the maximum slope during the upstroke.

No series resistance compensation was used. Series resistance did not exceed 20 MΩ. As provided in **Dataset S2**, mean resting membrane potential was –74.65 ± 1.02 mV, mean series resistance was 11.11 ± 0.40 MΩ, and mean membrane resistance was 71.14 ± 5.94 MΩ for PV$^{Cre/WT}$ animals; –74.09 ± 1.36 mV, 11.18 ± 0.56 MΩ, and 67.37 ± 5.86 MΩ for Kcng4$^{Cre/WT}$ animals; and –73.55 ± 0.88 mV, 10.71 ± 0.36 MΩ, and 63.94 ± 5.78 MΩ for Kcng4$^{Cre/Cre}$ animals.

Synaptic properties

For whole-cell voltage-clamp recordings assessing synaptic properties, patch pipettes were filled with high chloride cesium-based internal solution (in mM): 125 CsCl, 10 TEA-Cl, 10 HEPES, 0.1 EGTA, 3.3 QX-314, 1.8 $MgCl_2$, 4 Mg-ATP, 0.3 Na-GTP, and 8 Na_2Phosphocreatine (pH 7.3 adjusted with CsOH, 290–300 mOsm kg^{-1}). The following synaptic blockers were bath-applied: NBQX (10 µM, Tocris) and CPP (10 µM, Tocris). Signals were filtered at 10 kHz and digitized at 10 kHz.

Cells in PV–PYR pairs were typically < 50 µm apart. Action potentials were evoked in PV neurons at the minimal current injection required between 1–2 nA (1 ms) to elicit a postsynaptic current in the PYR neuron. Absolute amplitude was measured shortly after breaking in via 3–5 single action potential stimulation pulses. Afterwards, eleven distinct action potential stimulation patterns were applied, each of which was repeated 3–5 times per paired recording in a randomized order. For analysis of paired-pulse recordings, overlap between the first and second IPSCs was corrected by subtracting the residual decay of the first IPSC from the peak of the second IPSC. No correction was applied to 5-pulse trains.

Again, no series resistance compensation was used during the experiment. Series resistance did not exceed 30 MΩ. For all paired recordings, holding current did not exceed 200 pA at −70 mV. Mean series resistance was 18.93 ± 0.90 MΩ and mean membrane resistance was 210.90 ± 20.50 MΩ for PYR neurons recorded from $PV^{Cre/WT}$ animals; mean series resistance was 20.40 ± 1.51 MΩ and mean membrane resistance was 204.11 ± 11.80 MΩ for PYR neurons recorded from $Kcng4^{Cre/Cre}$ animals.

IPSC peak amplitude was converted to conductance according to established procedures to compensate for variability in parameters such as series resistance and membrane resistance (64). Given that we are only measuring inhibitory current $g_i(t)$ and there is no excitatory current $g_e(t)$:

$$g_{syn}(t) = g_e(t) + g_i(t) = g_i(t)$$

We used the following three equations to solve for $g_i(t)$:

$$I_i(t) = g_i(t)[V(t) - E_i(t)] \quad (1)$$
$$V(t) = V_{hold} - I(t)R_{series} \quad (2)$$
$$I(t) = I_i(t) + \frac{[V(t) - E_{rest}]}{R_{membrane}} \quad (3)$$

We derived the following equation for $g_i(t)$:

$$g_i(t) = \frac{E_{rest}}{R_{membrane}(V_{hold} - I(t)R_{series} - E_i)} \quad (4)$$

We measured $R_{membrane}$ and R_{series} from a test pulse during the recording, and we separately measured E_{rest} (–16 mV) and E_i (–2.5 mV). The PYR neuron was held at –70 mV; thus V_{hold} = –70 mV. Using these parameters, we converted inhibitory current I(t) to conductance $g_i(t)$.

Quantification and statistical analysis

Data is plotted as mean ± SEM. P values are represented as * for P < 0.05 and ** P < 0.005, and details regarding the *p* values and statistical tests are provided in the figure legends and supplementary files.

Data, materials, and software availability

All study data are included in the article and/or SI Appendix. The original code used to analyze the data in this study is publicly available on GitHub: https://github.com/sanikaganesh/IntrinSynC. Any additional information regarding the data and analysis is available from the lead contact upon request.

Acknowledgments

We thank all members of the Sabatini lab for helpful advice and technical assistance. We are grateful to W. Wang for advice on electrophysiology experiments. We thank C. King for mouse colony management and assistance with blinding the experimenter to mouse genotypes. We also thank C. Chen, W. Regehr, G. Fishell, and M. Andermann for useful insights. Additionally, we thank M. Ocana, M. EL-Rifai, and the Neurobiology Imaging Facility at Harvard Medical School for collaborating with our lab to complete the FISH experiments. We are especially grateful to M. Sherman, J. Wallace, W. Wang, T. Kula, J. McMahon, S. Liu, A. Girasole, and K. Mastro for feedback on the manuscript.

This work was supported by NIH R35NS137336 (to B.L.S), National Science Foundation Graduate Research Fellowship Program (NSF–GRFP) DGE 2140743 (to S.G.) and the Herchel Smith Graduate Fellowship (to S.G.).

691 **References**
692

693 1. E. S. Lein, *et al.*, Genome-wide atlas of gene expression in the adult mouse brain. *Nature* **445**,
694 168–176 (2007).

695 2. B. Tasic, *et al.*, Adult mouse cortical cell taxonomy revealed by single cell transcriptomics. *Nat.*
696 *Neurosci.* **19**, 335–346 (2016).

697 3. S. Hrvatin, *et al.*, Single-cell analysis of experience-dependent transcriptomic states in the
698 mouse visual cortex. *Nat Neurosci* **21**, 120–129 (2018).

699 4. B. Tasic, *et al.*, Shared and distinct transcriptomic cell types across neocortical areas. *Nature*
700 **563**, 72–78 (2018).

701 5. A. Saunders, *et al.*, Molecular Diversity and Specializations among the Cells of the Adult
702 Mouse Brain. *Cell* **174**, 1015-1030.e16 (2018).

703 6. V. Kozareva, *et al.*, A transcriptomic atlas of mouse cerebellar cortex comprehensively defines
704 cell types. *Nature* **598**, 214–219 (2021).

705 7. Z. Yao, *et al.*, A taxonomy of transcriptomic cell types across the isocortex and hippocampal
706 formation. *Cell* **184**, 3222-3241.e26 (2021).

707 8. Z. Yao, *et al.*, A transcriptomic and epigenomic cell atlas of the mouse primary motor cortex.
708 *Nature* **598**, 103–110 (2021).

709 9. J. Langlieb, *et al.*, The molecular cytoarchitecture of the adult mouse brain. *Nature* **624**, 333–
710 342 (2023).

711 10. M. Zhang, *et al.*, Molecularly defined and spatially resolved cell atlas of the whole mouse
712 brain. *Nature* **624**, 343–354 (2023).

713 11. H. Hu, J. Gan, P. Jonas, Fast-spiking, parvalbumin+ GABAergic interneurons: From cellular
714 design to microcircuit function. *Science* **345**, 1255263 (2014).

715 12. B. V. Atallah, W. Bruns, M. Carandini, M. Scanziani, Parvalbumin-Expressing Interneurons
716 Linearly Transform Cortical Responses to Visual Stimuli. *Neuron* **73**, 159–170 (2012).

717 13. N. R. Wilson, C. A. Runyan, F. L. Wang, M. Sur, Division and subtraction by distinct cortical
718 inhibitory networks in vivo. *Nature* **488**, 343–348 (2012).

719 14. M. Xue, B. V. Atallah, M. Scanziani, Equalizing excitation–inhibition ratios across visual
720 cortical neurons. *Nature* **511**, 596–600 (2014).

721 15. F. Pouille, M. Scanziani, Enforcement of Temporal Fidelity in Pyramidal Cells by Somatic
722 Feed-Forward Inhibition. *Science* **293**, 1159–1163 (2001).

723 16. J. A. Cardin, *et al.*, Driving fast-spiking cells induces gamma rhythm and controls sensory
724 responses. *Nature* **459**, 663–667 (2009).

725 17. A. Maffei, K. Nataraj, S. B. Nelson, G. G. Turrigiano, Potentiation of cortical inhibition by
726 visual deprivation. *Nature* **443**, 81–84 (2006).

727 18. M. A. Gainey, J. W. Aman, D. E. Feldman, Rapid Disinhibition by Adjustment of PV Intrinsic
728 Excitability during Whisker Map Plasticity in Mouse S1. *J Neurosci* **38**, 4749–4761 (2018).

729 19. T. K. Hensch, Critical period plasticity in local cortical circuits. *Nat. Rev. Neurosci.* **6**, 877–888
730 (2005).

731 20. O. Marín, Interneuron dysfunction in psychiatric disorders. *Nat. Rev. Neurosci.* **13**, 107–120
732 (2012).

733 21. A. Erisir, D. Lau, B. Rudy, C. S. Leonard, Function of Specific K+ Channels in Sustained
734 High-Frequency Firing of Fast-Spiking Neocortical Interneurons. *J. Neurophysiol.* **82**, 2476–2489
735 (1999).

736 22. B. Rudy, C. J. McBain, Kv3 channels: voltage-gated K+ channels designed for high-frequency
737 repetitive firing. *Trends Neurosci.* **24**, 517–526 (2001).

738 23. C.-C. Lien, P. Jonas, Kv3 Potassium Conductance is Necessary and Kinetically Optimized for
739 High-Frequency Action Potential Generation in Hippocampal Interneurons. *J. Neurosci.* **23**, 2058–
740 2068 (2003).

741 24. E. M. Goldberg, *et al.*, K+ Channels at the Axon Initial Segment Dampen Near-Threshold
742 Excitability of Neocortical Fast-Spiking GABAergic Interneurons. *Neuron* **58**, 387–400 (2008).

743 25. K.-X. Li, *et al.*, Neuregulin 1 regulates excitability of fast-spiking neurons through Kv1.1 and
744 acts in epilepsy. *Nat. Neurosci.* **15**, 267–273 (2012).

745 26. N. Dehorter, *et al.*, Tuning of fast-spiking interneuron properties by an activity-dependent
746 transcriptional switch. *Science* **349**, 1216–1220 (2015).

747 27. E. Bocksteins, D. J. Snyders, Electrically Silent Kv Subunits: Their Molecular and Functional
748 Characteristics. *Physiology* **27**, 73–84 (2012).

749 28. E. Bocksteins, Kv5, Kv6, Kv8, and Kv9 subunits: No simple silent bystanders. *J. Gen. Physiol.*
750 **147**, 105–125 (2016).

751 29. E. Bocksteins, *et al.*, Conserved Negative Charges in the N-terminal Tetramerization Domain
752 Mediate Efficient Assembly of Kv2.1 and Kv2.1/Kv6.4 Channels*. *J Biol Chem* **284**, 31625–31634
753 (2009).

754 30. E. Bocksteins, A. J. Labro, D. J. Snyders, D. P. Mohapatra, The Electrically Silent Kv6.4
755 Subunit Confers Hyperpolarized Gating Charge Movement in Kv2.1/Kv6.4 Heterotetrameric
756 Channels. *Plos One* **7**, e37143 (2012).

757 31. E. Bocksteins, D. J. Snyders, M. Holmgren, Independent movement of the voltage sensors in
758 KV2.1/KV6.4 heterotetramers. *Sci. Rep.* **7**, 41646 (2017).

759 32. M. C. Lee, *et al.*, Human Labor Pain Is Influenced by the Voltage-Gated Potassium Channel
760 KV6.4 Subunit. *Cell Rep.* **32**, 107941 (2020).

761 33. L. Möller, G. Regnier, A. J. Labro, R. Blunck, D. J. Snyders, Determining the correct
762 stoichiometry of Kv2.1/Kv6.4 heterotetramers, functional in multiple stoichiometrical
763 configurations. *Proc. Natl. Acad. Sci.* **117**, 9365–9376 (2020).

764 34. G. Lacroix, S. Bhat, Z. Shafia, R. Blunck, KCNG4 Genetic Variant Linked to Migraine
765 Prevents Expression of KCNB1. *Int. J. Mol. Sci.* **25**, 8960 (2024).

766 35. D. Tewari, C. Sattler, K. Benndorf, Functional properties of a disease mutation for migraine in
767 Kv2.1/6.4 channels. *Biochem. Biophys. Res. Commun.* **738**, 150560 (2024).

768 36. T. A. Lacey, K. D. Murray, J. S. Trimmer, J. T. Sack, M. J. Ferns, Kv2/Kv6.4 Heteromeric
769 Potassium Channels Are Expressed in Spinal Motoneurons and Localized at C-Bouton
770 Synapses. *Eur. J. Neurosci.* **62**, e70243 (2025).

771 37. Q. Cui, *et al.*, Dissociable Roles of Pallidal Neuron Subtypes in Regulating Motor Patterns. *J*
772 *Neurosci* **41**, 4036–4059 (2021).

773 38. J.-P. David, J. I. Stas, N. Schmitt, E. Bocksteins, Auxiliary KCNE subunits modulate both
774 homotetrameric Kv2.1 and heterotetrameric Kv2.1/Kv6.4 channels. *Sci. Rep.* **5**, 12813 (2015).

775 39. H. I. Bishop, *et al.*, Distinct Cell- and Layer-Specific Expression Patterns and Independent
776 Regulation of Kv2 Channel Subtypes in Cortical Pyramidal Neurons. *J. Neurosci.* **35**, 14922–
777 14942 (2015).

778 40. Y. Kobayashi, Z. Ye, T. K. Hensch, Clock Genes Control Cortical Critical Period Timing.
779 *Neuron* **86**, 264–275 (2015).

780 41. B. P. Bean, The action potential in mammalian central neurons. *Nat. Rev. Neurosci.* **8**, 451–
781 465 (2007).

782 42. B. Wang, *et al.*, Firing Frequency Maxima of Fast-Spiking Neurons in Human, Monkey, and
783 Mouse Neocortex. *Front. Cell. Neurosci.* **10**, 239 (2016).

784 43. J. Du, L. L. Haak, E. Phillips-Tansey, J. T. Russell, C. J. McBain, Frequency-dependent
785 regulation of rat hippocampal somato-dendritic excitability by the K+ channel subunit Kv2.1. *J.*
786 *Physiol.* **522**, 19–31 (2000).

787 44. H. Misonou, D. P. Mohapatra, J. S. Trimmer, Kv2.1: A Voltage-Gated K+ Channel Critical to
788 Dynamic Control of Neuronal Excitability. *NeuroToxicology* **26**, 743–752 (2005).

789 45. P. W. Liu, B. P. Bean, Kv2 Channel Regulation of Action Potential Repolarization and Firing
790 Patterns in Superior Cervical Ganglion Neurons and Hippocampal CA1 Pyramidal Neurons. *J.*
791 *Neurosci.* **34**, 4991–5002 (2014).

792 46. B. L. Sabatini, W. G. Regehr, Control of Neurotransmitter Release by Presynaptic Waveform
793 at the Granule Cell to Purkinje Cell Synapse. *J. Neurosci.* **17**, 3425–3435 (1997).

794 47. J. G. G. Borst, B. Sakmann, Effect of changes in action potential shape on calcium currents
795 and transmitter release in a calyxtype synapse of the rat auditory brainstem. *Philos. Trans. R.*
796 *Soc. Lond. Ser. B: Biol. Sci.* **354**, 347–355 (1999).

797 48. J. R. P. Geiger, P. Jonas, Dynamic Control of Presynaptic Ca2+ Inflow by Fast-Inactivating
798 K+ Channels in Hippocampal Mossy Fiber Boutons. *Neuron* **28**, 927–939 (2000).

799 49. E. M. Goldberg, *et al.*, Specific Functions of Synaptically Localized Potassium Channels in
800 Synaptic Transmission at the Neocortical GABAergic Fast-Spiking Cell Synapse. *J Neurosci* **25**,
801 5230–5235 (2005).

802 50. D. Vormstein-Schneider, *et al.*, Viral manipulation of functionally distinct interneurons in mice,
803 non-human primates and humans. *Nat Neurosci* **23**, 1629–1636 (2020).

804 51. A. M. Packer, R. Yuste, Dense, Unspecific Connectivity of Neocortical Parvalbumin-Positive
805 Interneurons: A Canonical Microcircuit for Inhibition? *J. Neurosci.* **31**, 13260–13271 (2011).

806 52. D. E. Feldman, M. Brecht, Map Plasticity in Somatosensory Cortex. *Science* **310**, 810–815
807 (2005).

808 53. P. W. E. Spratt, *et al.*, The Autism-Associated Gene Scn2a Contributes to Dendritic
809 Excitability and Synaptic Function in the Prefrontal Cortex. *Neuron* **103**, 673-685.e5 (2019).

810 54. T. Karayannis, *et al.*, Cntnap4 differentially contributes to GABAergic and dopaminergic
811 synaptic transmission. *Nature* **511**, 236–240 (2014).

812 55. V. J. Olah, *et al.*, Biophysical Kv3 channel alterations dampen excitability of cortical PV
813 interneurons and contribute to network hyperexcitability in early Alzheimer's. *Elife* **11**, e75316
814 (2022).

815 56. R. G. Stewart, *et al.*, A Kv2 inhibitor combination reveals native neuronal conductances
816 consistent with Kv2/KvS heteromers. *eLife* **13**, RP99410 (2025).

817 57. G. Regnier, *et al.*, Targeted deletion of the Kv6.4 subunit causes male sterility due to
818 disturbed spermiogenesis. *Reprod., Fertil. Dev.* **29**, 1567 (2016).

819 58. H. Shen, E. Bocksteins, I. Kondrychyn, D. Snyders, V. Korzh, Functional antagonism of
820 voltage-gated K+ channel α-subunits in the developing brain ventricular system. *Development*
821 **143**, 4249–4260 (2016).

822 59. J. Jędrychowska, V. Korzh, Kv2.1 voltage-gated potassium channels in developmental
823 perspective. *Dev. Dyn.* **248**, 1180–1194 (2019).

824 60. C. G. F. de Kovel, *et al.*, Neurodevelopmental Disorders Caused by De Novo Variants in
825 KCNB1 Genotypes and Phenotypes. *JAMA Neurol.* **74**, 1228 (2017).

826 61. M. Kessi, *et al.*, Intellectual Disability and Potassium Channelopathies: A Systematic Review.
827 *Front. Genet.* **11**, 614 (2020).

828 62. N. M. Allen, S. Weckhuysen, K. Gorman, M. D. King, H. Lerche, Genetic potassium channel-
829 associated epilepsies: Clinical review of the Kv family. *Eur. J. Paediatr. Neurol.* **24**, 105–116
830 (2020).

831 63. D. J. Speca, *et al.*, Deletion of the Kv2.1 delayed rectifier potassium channel leads to
832 neuronal and behavioral hyperexcitability. *Genes, Brain Behav.* **13**, 394–408 (2014).

833 64. M. Wehr, A. M. Zador, Balanced inhibition underlies tuning and sharpens spike timing in
834 auditory cortex. *Nature* **426**, 442–446 (2003).

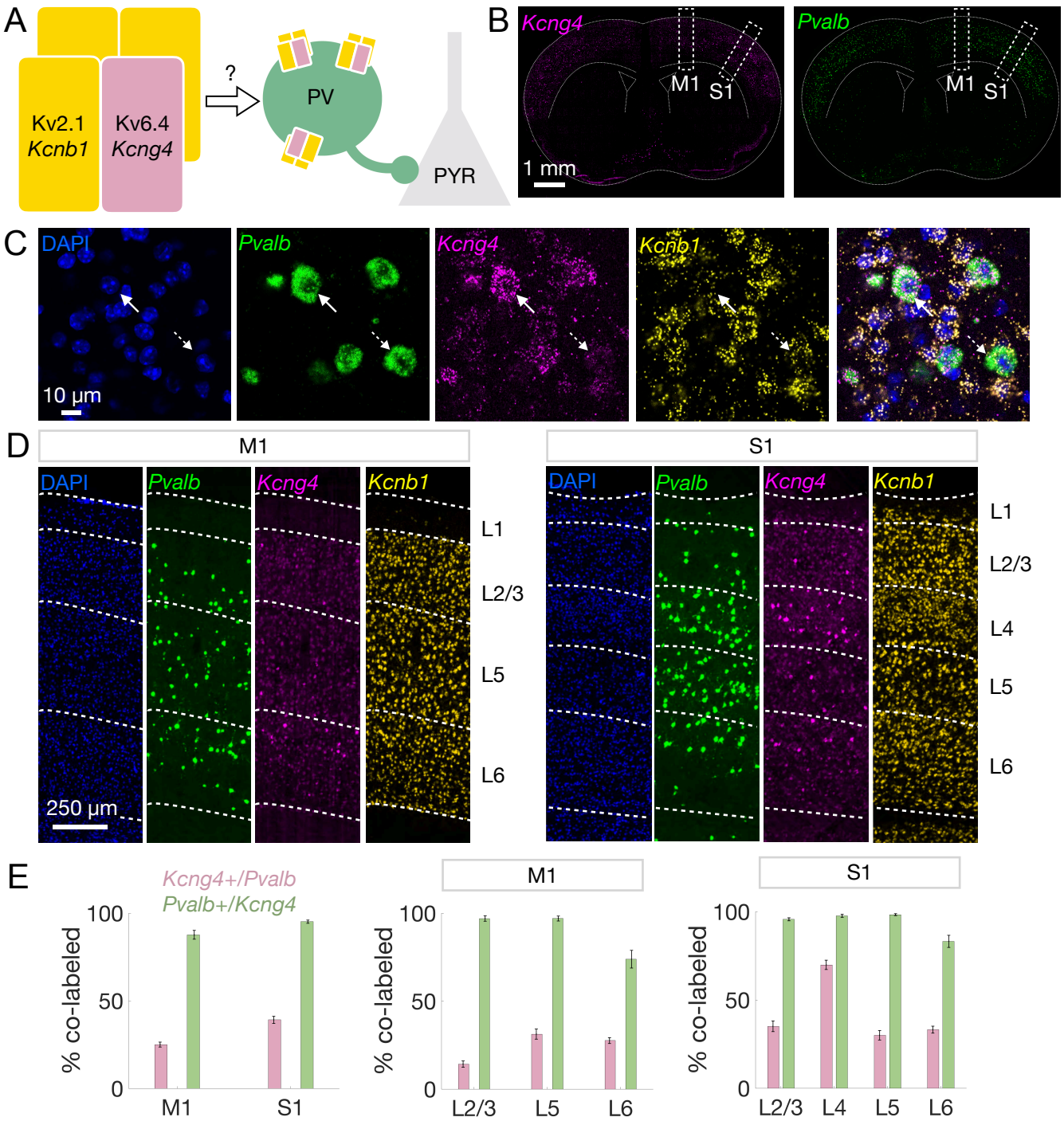
A
Kv2.1
Kcnb1
Kv6.4
Kcng4
?
PV
PYR
B
Kcng4
Pvalb
M1
S1
1 mm
C
DAPI
Pvalb
Kcng4
Kcnb1
10 µm
D
M1
S1
DAPI
Pvalb
Kcng4
Kcnb1
L1
L2/3
L4
L5
L6
250 µm
E
Kcng4+/Pvalb
Pvalb+/Kcng4
% co-labeled
100
50
0
M1
S1
L2/3
L4
L5
L6

Fig. 1. Cortical PV neurons selectively express *Kcng4*.
A, Schematic illustrating the hypothesis that Kv6.4 (encoded by *Kcng4*) confers cell-type-specific function by forming heterotetrameric channels with Kv2.1 (encoded by *Kcnb1*). We tested whether Kv6.4 modulates PV neuron excitability and PV inhibition of excitatory pyramidal (PYR) neurons.
B, Coronal brain sections displaying the spatial distribution of *Kcng4* (magenta, *left*) and *Pvalb* (green, *right*) mRNA across cortex detected by FISH. Subsequent analyses focus on primary motor (M1) and somatosensory (S1) cortical regions, indicated by white dashed boxes.
C, Representative images of individual cortical cells labeled with DAPI (blue) and FISH against *Pvalb* (green), *Kcng4* (magenta), and *Kcnb1* (yellow), followed by a merged view (*left* to *right*). Solid white arrows indicate a cell that co-expresses *Pvalb, Kcnb1,* and *Kcng4*, and dashed white arrows indicate a cell that co-expresses *Pvalb* and *Kcnb1*.
D, Representative images of M1 and S1 showing the spatial distribution of *Kcng4*, *Pvalb*, and *Kcnb1* mRNA. White dashed lines and text labels denote individual cortical layers (L).
E, Quantification of co-labeled cells displaying the percentage of *Pvalb*-expressing cells that are *Kcng4*+ (pink) and the percentage of *Kcng4*-expressing cells that are *Pvalb*+ (green) in M1 and S1 (n = 6 mice with 18 sections and 36 hemispheres per region, 2–4 sections per mouse) across all layers (*left*). Quantification by cortical layer in M1 (*center*) and S1 (*right*).
Mean ± SEM displayed.

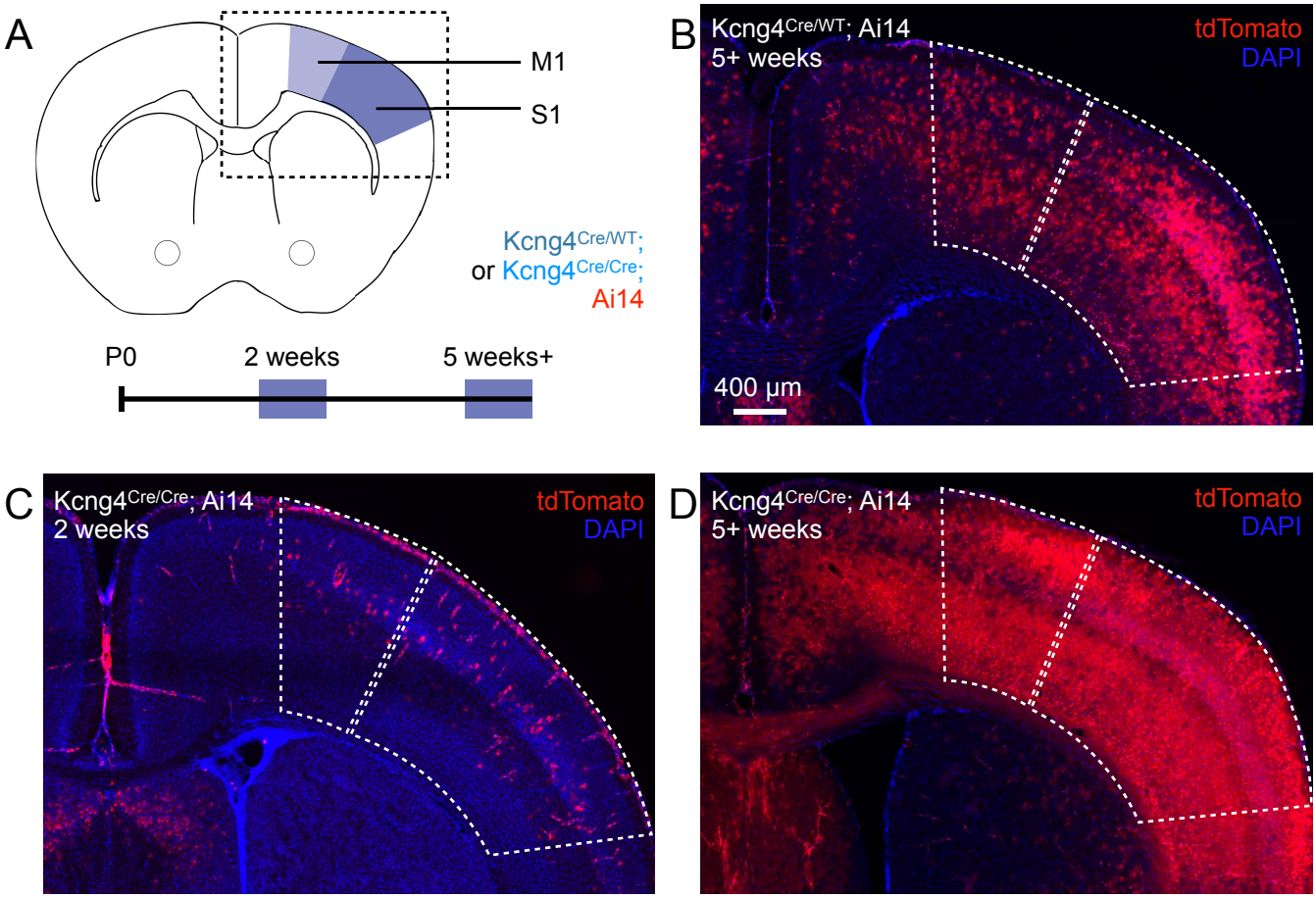
A
M1
S1
Kcng4Cre/WT;
or Kcng4Cre/Cre;
Ai14
P0
2 weeks
5 weeks+
B
Kcng4Cre/WT; Ai14
5+ weeks
tdTomato
DAPI
400 µm
C
Kcng4Cre/Cre; Ai14
2 weeks
tdTomato
DAPI
D
Kcng4Cre/Cre; Ai14
5+ weeks
tdTomato
DAPI

Fig. 2. Age dependence of Kcng4^{Cre} activation.
A, Schematic of the brain regions analyzed to assess Kcng4^{Cre} activation at juvenile (2 weeks) and adult (5+ weeks) timepoints in heterozygous (Kcng4$^{Cre/WT}$; Ai14) and homozygous (Kcng4$^{Cre/Cre}$; Ai14) mice. Analyses focused on primary motor (M1) and somatosensory (S1) cortex, as indicated.
B–D, Representative images showing tdTomato fluorescence in M1 and S1, as indicated in panel A, for Kcng4$^{Cre/WT}$; Ai14 mice at 5+ weeks **(B)**, and Kcng4$^{Cre/Cre}$; Ai14 mice at 2 weeks **(C)** and 5+ weeks **(D)**.

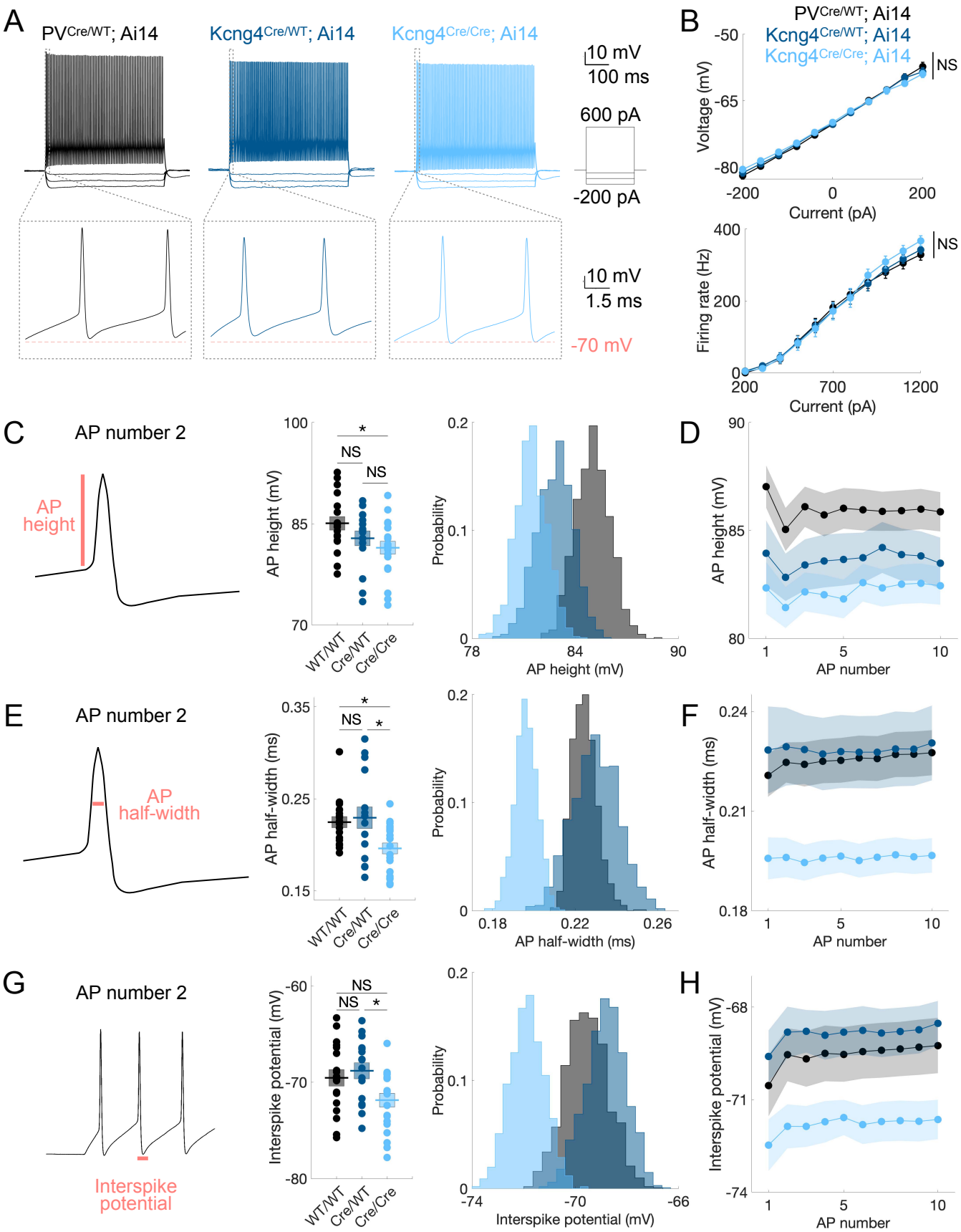
A
PVCre/WT; Ai14
Kcng4Cre/WT; Ai14
Kcng4Cre/Cre; Ai14
10 mV
100 ms
600 pA
-200 pA
10 mV
1.5 ms
-70 mV
B
PVCre/WT; Ai14
Kcng4Cre/WT; Ai14
Kcng4Cre/Cre; Ai14
NS
Voltage (mV)
Current (pA)
Firing rate (Hz)
Current (pA)
C
AP number 2
AP height
AP height (mV)
WT/WT
Cre/WT
Cre/Cre
Probability
AP height (mV)
D
AP height (mV)
AP number
E
AP number 2
AP half-width
AP half-width (ms)
Probability
AP half-width (ms)
F
AP half-width (ms)
AP number
G
AP number 2
Interspike potential
Interspike potential (mV)
Probability
Interspike potential (mV)
H
Interspike potential (mV)
AP number

Fig. 3. Kv6.4 modulates AP height, AP half-width, and interspike potential in PV neurons.
A, Representative whole-cell current-clamp recordings from L2/3 fast-spiking neurons in S1 of mice with two ($PV^{Cre/WT}$; Ai14), one ($Kcng4^{Cre/WT}$; Ai14), and no ($Kcng4^{Cre/Cre}$; Ai14) active alleles of *Kcng4*. Voltage responses to a series of current injections (–200, –120, –40, and 600 pA) are shown in the top row. An expanded view of the first two action potentials in response to a 600 pA current injection is shown in the bottom row, aligned to a membrane potential of –70 mV.
B, Voltage (mV, *top*) and firing rate (Hz, *bottom*) responses to stepwise current injections for wildtype (n = 18 cells in 4 mice), heterozygous (n = 16 cells in 4 mice), and homozygous (n = 20 cells in 4 mice) groups.
C, Schematic of action potential (AP) height (*left*) and its group mean measured for the 2nd AP (mV, *center*) in the first current step that elicited at least 10 APs. Bootstrapped distribution of the means (*right*).
D, Mean values across the first 10 APs (mV) in a response that elicited at least 10 APs.
E–H, As in **C** and **D** for AP half-width (ms) (**E-F**) and interspike potential (mV) (**G-H**).
Mean ± SEM displayed. * $P < 0.05$; NS: not statistically significant. Repeated-measures ANOVA (Greenhouse-Geisser corrected) or one-way ANOVA (with Tukey-Kramer multiple comparisons). Bootstrapping (1,000 iterations) was used to visualize sample mean distributions.

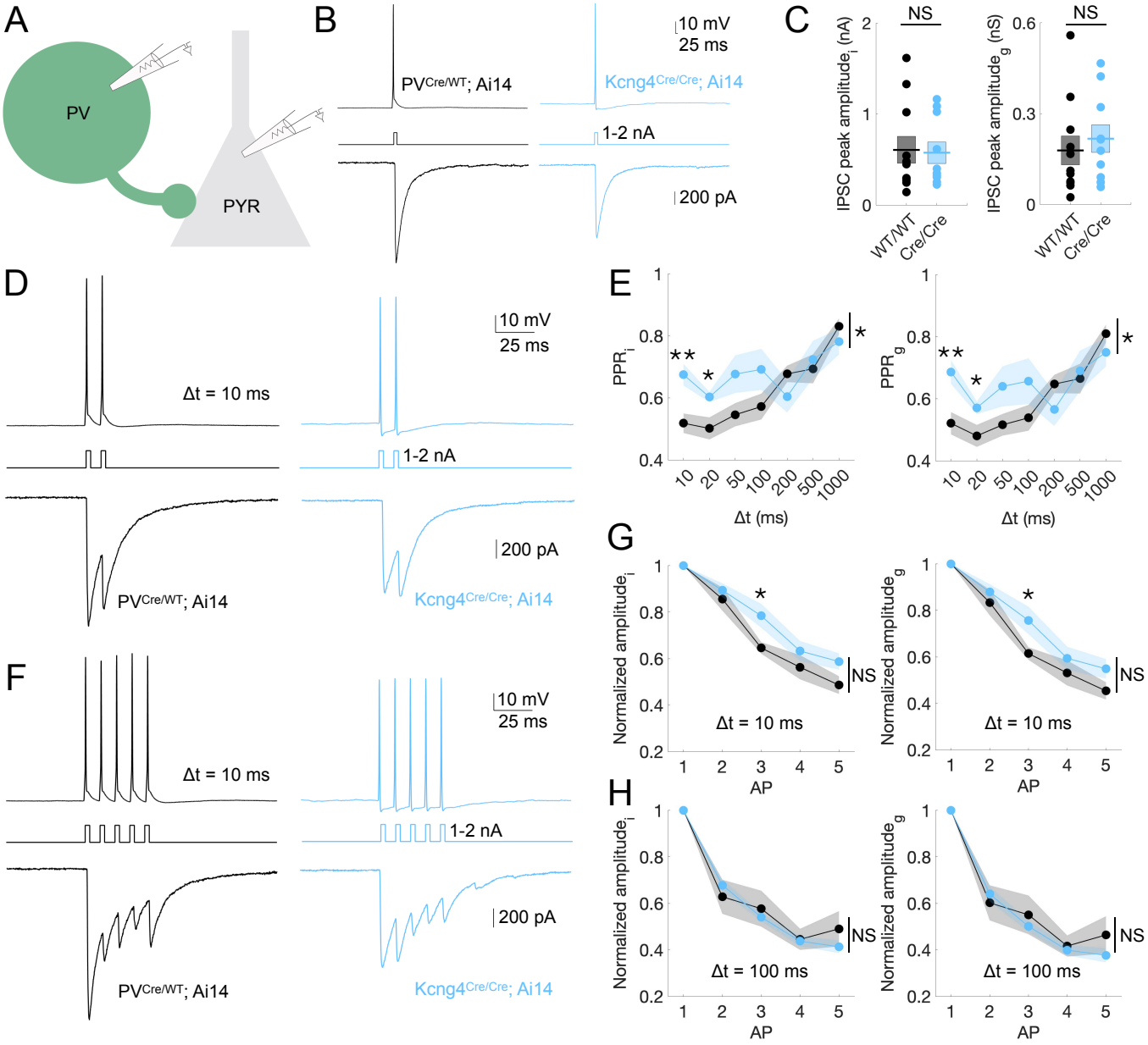
A
PV
PYR
B
PVCre/WT; Ai14
Kcng4Cre/Cre; Ai14
10 mV
25 ms
1-2 nA
200 pA
C
NS
IPSC peak amplitudei (nA)
IPSC peak amplitudeg (nS)
WT/WT
Cre/Cre
D
Δt = 10 ms
E
PPRi
PPRg
Δt (ms)
G
Normalized amplitudei
Normalized amplitudeg
AP
H
Δt = 100 ms

Fig. 4. Kv6.4 regulates paired-pulse depression at PV-PYR synapses during high-frequency AP firing.

A, Schematic of paired whole-cell recordings from PV and PYR neurons.

B, Representative whole-cell voltage-clamp recordings from L2/3 PYR neurons in S1 of mice with two ($PV^{Cre/WT}$; Ai14) and no ($Kcng4^{Cre/Cre}$; Ai14) active alleles of *Kcng4*. APs were evoked in tdTomato-positive, fast-spiking neurons by brief current injections (1–2 nA, 1 ms), resulting in inhibitory postsynaptic currents (IPSCs) in synaptically connected PYR neurons. A representative response to a single AP is displayed for each group.

C, IPSC peak amplitude measured as current (*i*; *left,* nA) or converted to conductance (*g*; *right,* nS) for wildtype (n = 11 pairs in 9 mice) and homozygous (n = 10 pairs in 8 mice) groups.

D, Representative response to two presynaptic action potentials (paired-pulse stimulation) delivered with an interstimulus interval of 10 ms, recorded as in **B**.

E, Paired-pulse ratio (PPR) of inhibitory current (*i*; *left*) and conductance (*g*; *right*) across groups for ISIs of 10, 20, 50, 100, 200, 500, and 1000 ms.

F, Representative response to five presynaptic action potentials delivered with an interstimulus interval of 10 ms, recorded as in **B** and **D**.

G, Amplitude of inhibitory current (*i*; *left*) and conductance (*g*; *right*) across groups, normalized to response from the first AP, for an ISI (Δt) of 10 ms.

H, As in **G** for an ISI of 100 ms.

Mean ± SEM displayed. ** $P < 0.005$, * $P < 0.05$; NS: not statistically significant. Unpaired two-tailed t-tests or repeated-measures ANOVA (Greenhouse-Geisser corrected).

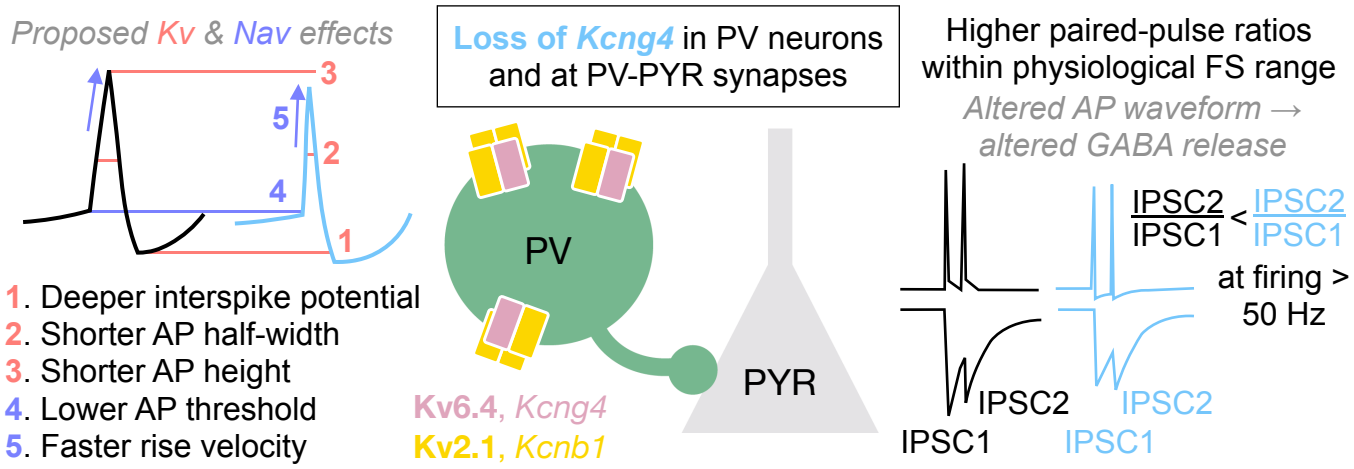
Proposed Kv & Nav effects
3
5
2
4
1
1. Deeper interspike potential
2. Shorter AP half-width
3. Shorter AP height
4. Lower AP threshold
5. Faster rise velocity
Loss of Kcng4 in PV neurons and at PV-PYR synapses
PV
PYR
Kv6.4, Kcng4
Kv2.1, Kcnb1
Higher paired-pulse ratios within physiological FS range
Altered AP waveform → altered GABA release
IPSC2/IPSC1 < IPSC2/IPSC1
at firing > 50 Hz
IPSC2
IPSC1
IPSC2
IPSC1

Figure 5. Model: Kv6.4 alters PV neuron waveform and inhibition of PYR neurons. Kv6.4 (*Kcng4*) forms heterotetrameric potassium channel complexes in PV neurons. The absence of Kv6.4 results in (1) deeper interspike potentials, (2) shorter AP half-width, and (3) shorter AP height, likely due to its effects on Kv2 currents. Loss of Kv6.4 also results in (4) lower AP threshold and (5) faster rise velocity, which we propose is due to a resulting increase in Nav channel availability. We propose that these waveform changes lead to an increase in paired-pulse ratios of inhibition evoked in postsynaptic PYR neurons at short interstimulus intervals. Thus, Kv6.4 regulates presynaptic GABA release during high-frequency firing and thereby regulates the temporal precision of PV inhibitory output.

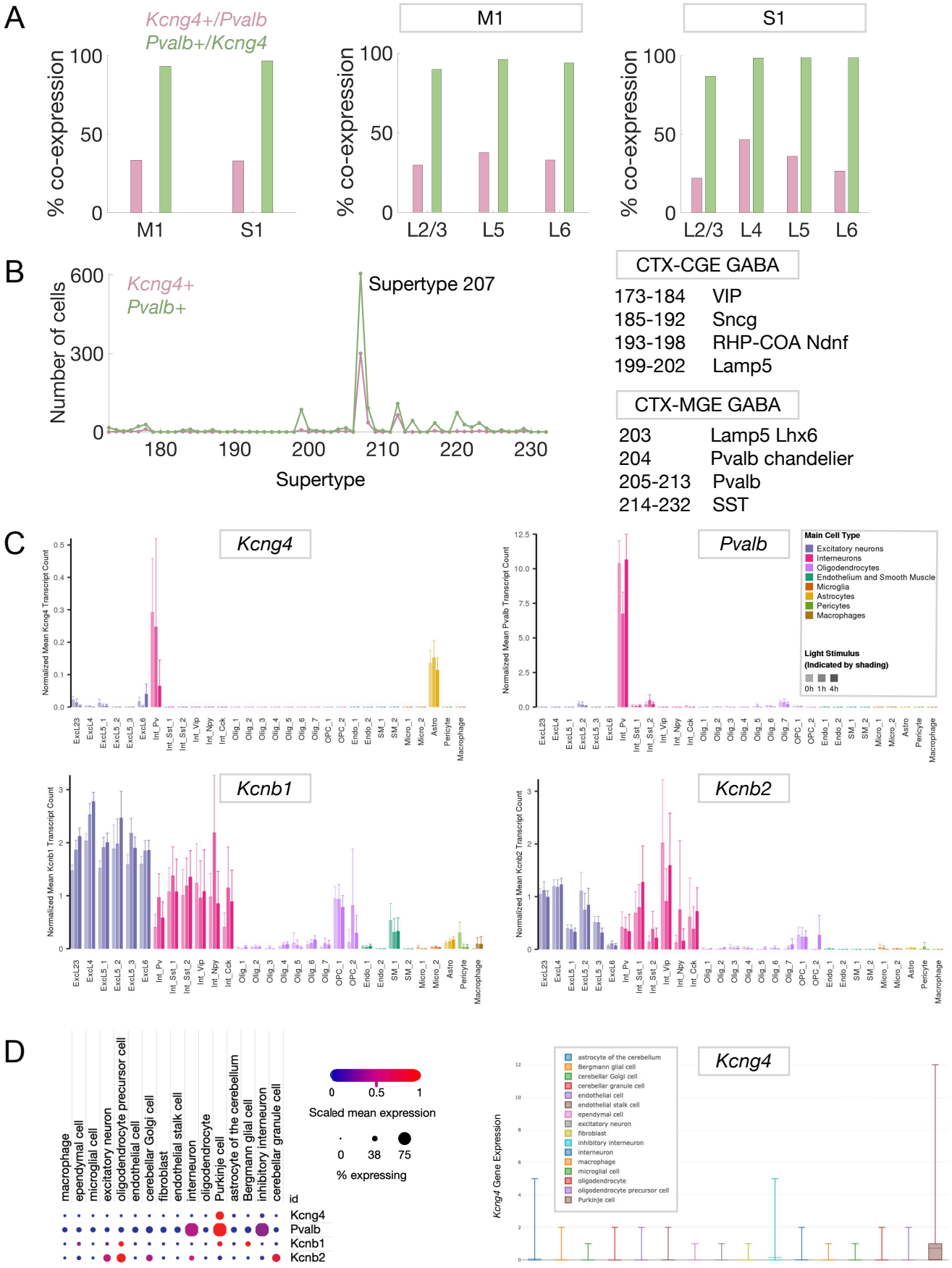
A
Kcng4+/Pvalb
Pvalb+/Kcng4
% co-expression
M1
S1
L2/3
L4
L5
L6
B
Kcng4+
Pvalb+
Number of cells
Supertype 207
Supertype
CTX-CGE GABA
173-184 VIP
185-192 Sncg
193-198 RHP-COA Ndnf
199-202 Lamp5
CTX-MGE GABA
203 Lamp5 Lhx6
204 Pvalb chandelier
205-213 Pvalb
214-232 SST
C
Kcng4
Pvalb
Kcnb1
Kcnb2
Normalized Mean Kcng4 Transcript Count
Normalized Mean Pvalb Transcript Count
Normalized Mean Kcnb1 Transcript Count
Normalized Mean Kcnb2 Transcript Count
Main Cell Type
Excitatory neurons
Interneurons
Oligodendrocytes
Endothelium and Smooth Muscle
Microglia
Astrocytes
Pericytes
Macrophages
Light Stimulus
(Indicated by shading)
0h 1h 4h
D
macrophage
ependymal cell
microglial cell
excitatory neuron
oligodendrocyte precursor cell
endothelial cell
cerebellar Golgi cell
fibroblast
endothelial stalk cell
interneuron
oligodendrocyte
Purkinje cell
astrocyte of the cerebellum
Bergmann glial cell
inhibitory interneuron
cerebellar granule cell
id
Kcng4
Pvalb
Kcnb1
Kcnb2
Scaled mean expression
% expressing
Kcng4 Gene Expression

Fig. S1. Co-expression and cell-type-specificity of *Kcng4* and *Pvalb* across spatial and single-cell transcriptomic datasets.

A, Quantification of cells co-expressing *Kcng4* and *Pvalb* in adult mouse cortex was performed using Multiplexed Error-Robust Fluorescence *In Situ* Hybridization (MERFISH) data from the Allen Brain Cell (ABC) Atlas (Zhuang-ABCA-1, MERFISH whole brain coronal 1), accessed via the Brain Knowledge Platform (10). Percentage of co-expressing cells in M1 and S1, labeling as in **Fig. 1E**.

B, Number of *Kcng4*- and *Pvalb*-expressing cells in S1 across PV neuron supertypes, as classified by the ABC Atlas (*left*). Legend detailing inhibitory subtypes (*right*). Abbreviations: CTX, cortex; CGE, caudal ganglionic eminence; MGE, medial ganglionic eminence; GABA, GABAergic neuron; VIP, vasoactive intestinal peptide; Sncg, synuclein, gamma; RHP, retrohippocampal region; COA, cortical amygdalar area; Ndnf, neuron-derived neurotrophic factor; Lamp5, lysosomal-associated membrane protein family, member 5; Lhx6, LIM homeobox protein 6; Pvalb, parvalbumin; SST, somatostatin.

C, Normalized transcript counts for *Kcng4*, *Pvalb*, *Kcnb1*, and *Kcnb2* across cell types in mouse adult visual cortex from single-cell RNA sequencing data (3) accessed via an interactive gene expression database.

D, Gene expression for *Kcng4*, *Pvalb*, *Kcnb1*, and *Kcnb2* across cell types in mouse adult cerebellar cortex from single-nuclei RNA sequencing data (6) with a detailed visualization of *Kcng4* gene expression, accessed via the interactive Single Cell Portal.

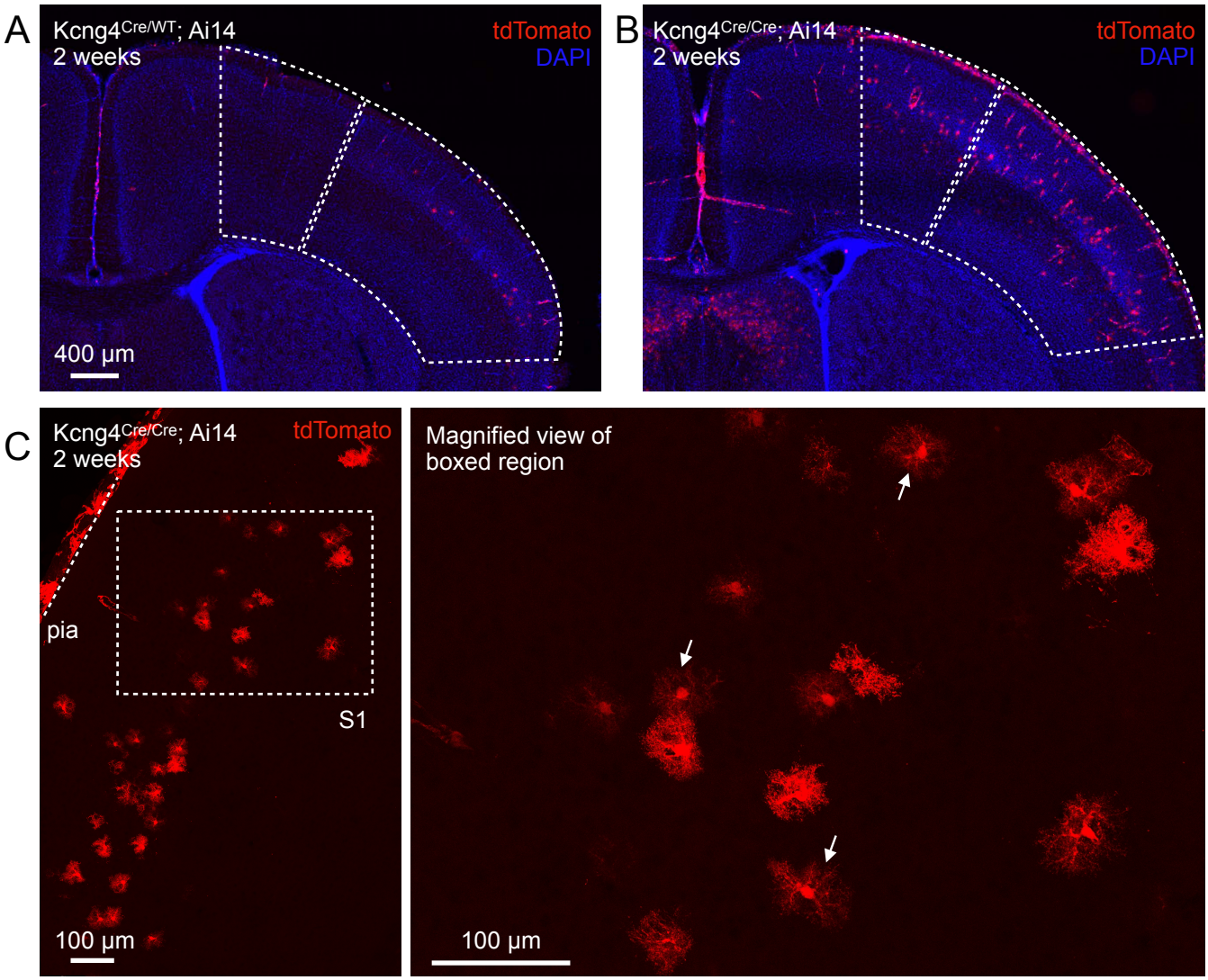
A
Kcng4Cre/WT; Ai14
2 weeks
tdTomato
DAPI
400 µm
B
Kcng4Cre/Cre; Ai14
2 weeks
tdTomato
DAPI
C
Kcng4Cre/Cre; Ai14
2 weeks
tdTomato
pia
S1
100 µm
Magnified view of
boxed region
100 µm

Fig. S2. Kcng4^{Cre} activation in juvenile mice.
A-B, Representative images showing tdTomato fluorescence in M1 and S1 for heterozygous (Kcng4$^{Cre/WT}$; Ai14) **(A)** and homozygous (Kcng4$^{Cre/Cre}$; Ai14) **(B)** mice at 2 weeks, corresponding to the regions outlined in **Fig. 2A**.
C, Higher magnification images illustrating the distribution of tdTomato-positive cells in S1 of a homozygous (Kcng4$^{Cre/Cre}$; Ai14) mouse. Magnified view (*right*) of the boxed region (*left*) marked by dashed white lines. Solid white arrows highlight example cells exhibiting astrocytic morphology (*right*).

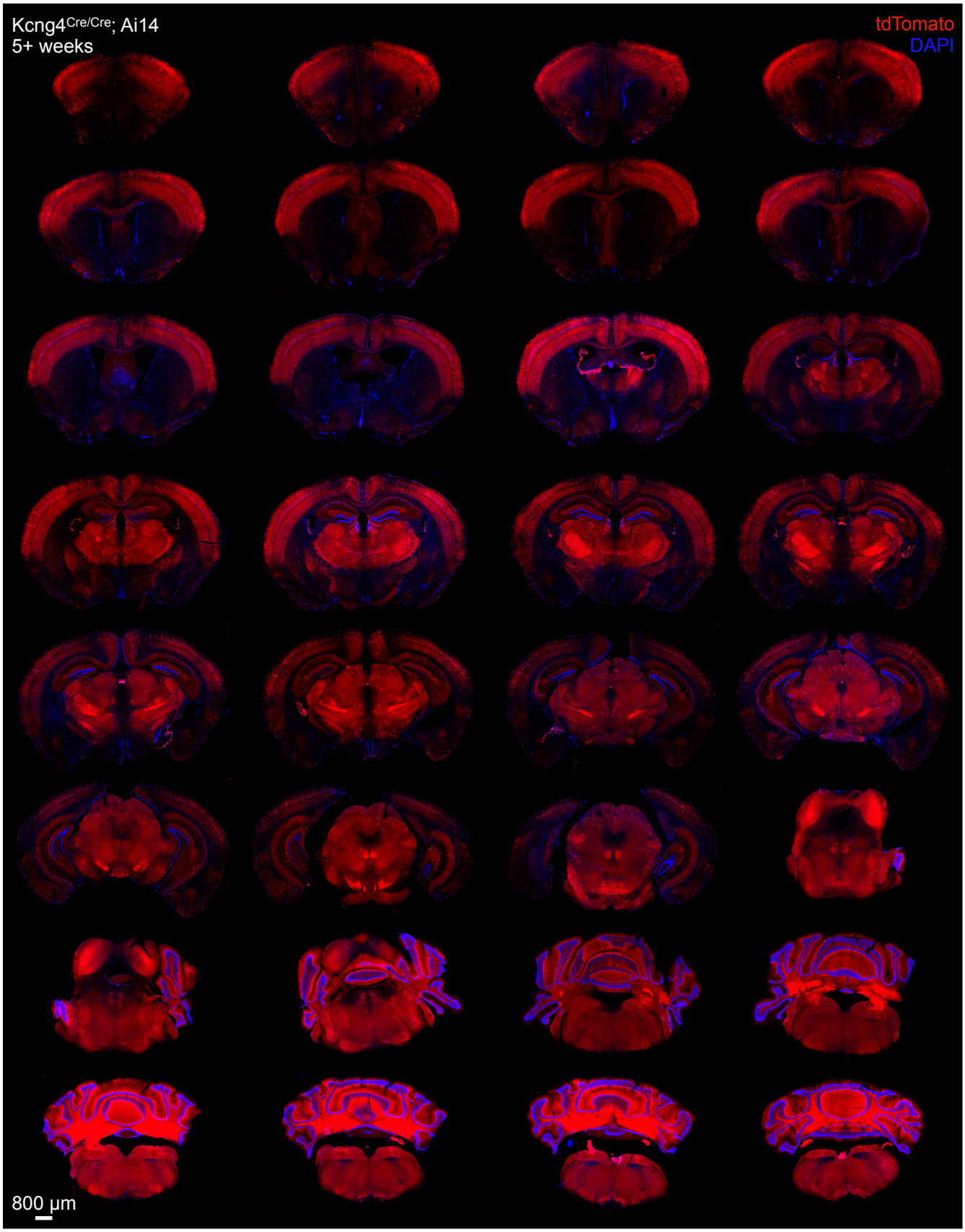
Kcng4Cre/Cre; Ai14
5+ weeks
tdTomato
DAPI
800 µm

Fig. S3. Brain-wide Kcng4^{Cre} activation in adult mice.
Representative images showing tdTomato fluorescence in a homozygous (Kcng4$^{Cre/Cre}$; Ai14) mouse at 5+ weeks across various brain areas, arranged anterior to posterior.

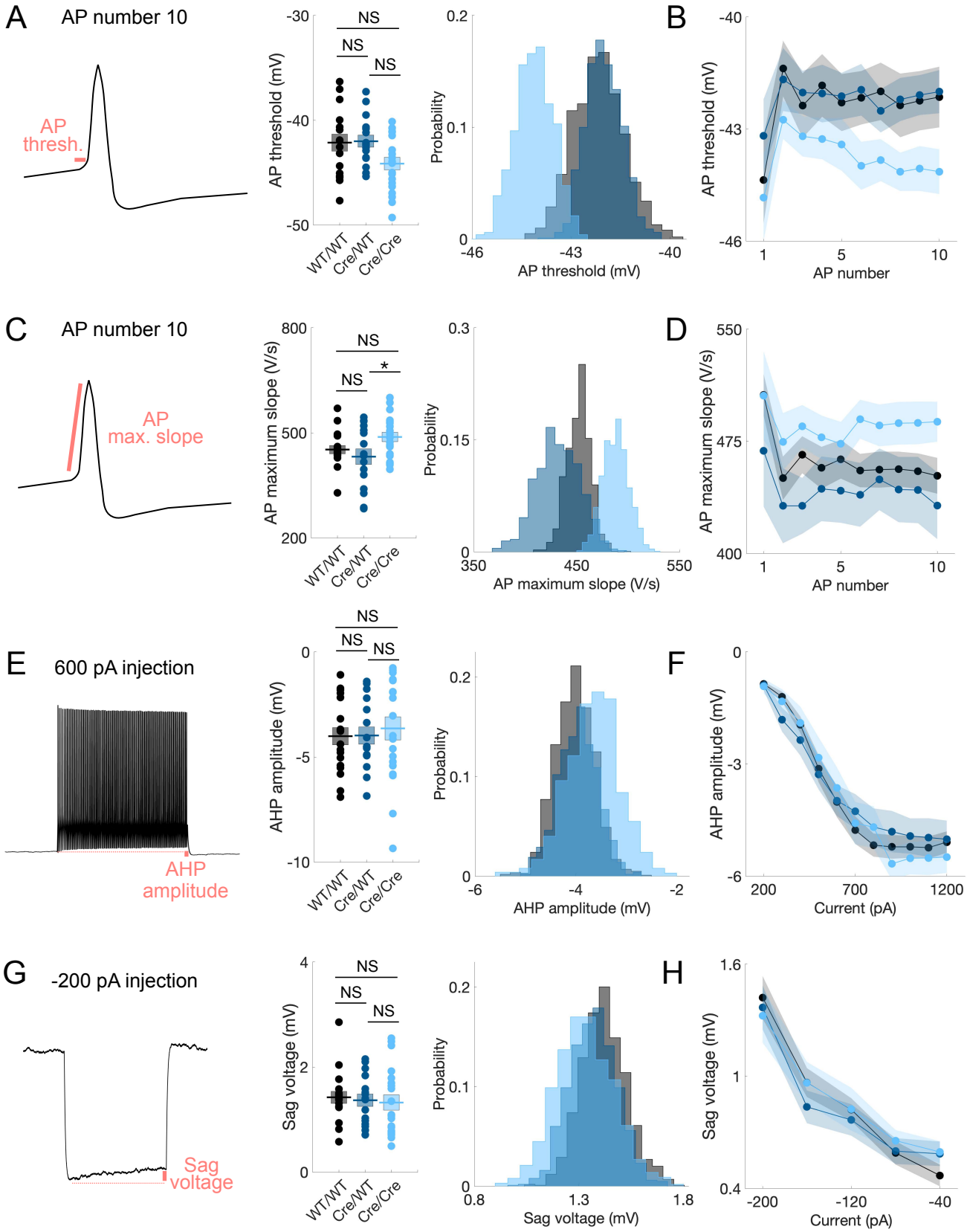
A
AP number 10
AP
thresh.
AP threshold (mV)
-30
-40
-50
NS
NS
NS
WT/WT
Cre/WT
Cre/Cre
Probability
0.2
0.1
0
-46
-43
-40
AP threshold (mV)
B
AP threshold (mV)
-40
-43
-46
1
5
10
AP number
C
AP number 10
AP
max. slope
AP maximum slope (V/s)
800
500
200
NS
NS
*
WT/WT
Cre/WT
Cre/Cre
Probability
0.3
0.15
0
350
450
550
AP maximum slope (V/s)
D
AP maximum slope (V/s)
550
475
400
1
5
10
AP number
E
600 pA injection
AHP
amplitude
AHP amplitude (mV)
0
-5
-10
NS
NS
NS
WT/WT
Cre/WT
Cre/Cre
Probability
0.2
0.1
0
-6
-4
-2
AHP amplitude (mV)
F
AHP amplitude (mV)
0
-3
-6
200
700
1200
Current (pA)
G
-200 pA injection
Sag
voltage
Sag voltage (mV)
4
2
0
NS
NS
NS
WT/WT
Cre/WT
Cre/Cre
Probability
0.2
0.1
0
0.8
1.3
1.8
Sag voltage (mV)
H
Sag voltage (mV)
1.6
1
0.4
-200
-120
-40
Current (pA)

Fig. S4. Additional intrinsic properties of PV neurons following Kv6.4 deletion.
A, Schematic of AP threshold (*left*), group means (mV, *center*), and bootstrapped distribution of the means (*right*) for the 10th AP, as described in **Fig. 3**.
B, Mean values across the first 10 APs (mV).
C-H, As in **A** and **B** for AP maximum slope (V/s) (**C-D**), afterhyperpolarization (AHP) amplitude (mV) (**E-F**), and sag voltage (mV) (**G-H**).
AHP amplitude was measured from a current injection of 600 pA (**E**) and across stepwise current injections from 200 to 1200 pA (**F**). AHP amplitude was defined as the difference between the resting membrane potential and the most negative voltage following current injection. Sag voltage was measured from a current injection of –200 pA (**G**) and across hyperpolarizing steps from –200 to –40 pA (**H**). Sag voltage was defined as the difference between the steady-state voltage and peak hyperpolarization during hyperpolarizing current injections.
Mean ± SEM displayed. * $P < 0.05$; NS: not statistically significant. One-way ANOVA (Tukey-Kramer post hoc multiple comparisons). Bootstrapping (1,000 iterations) was used to visualize sample mean distributions.

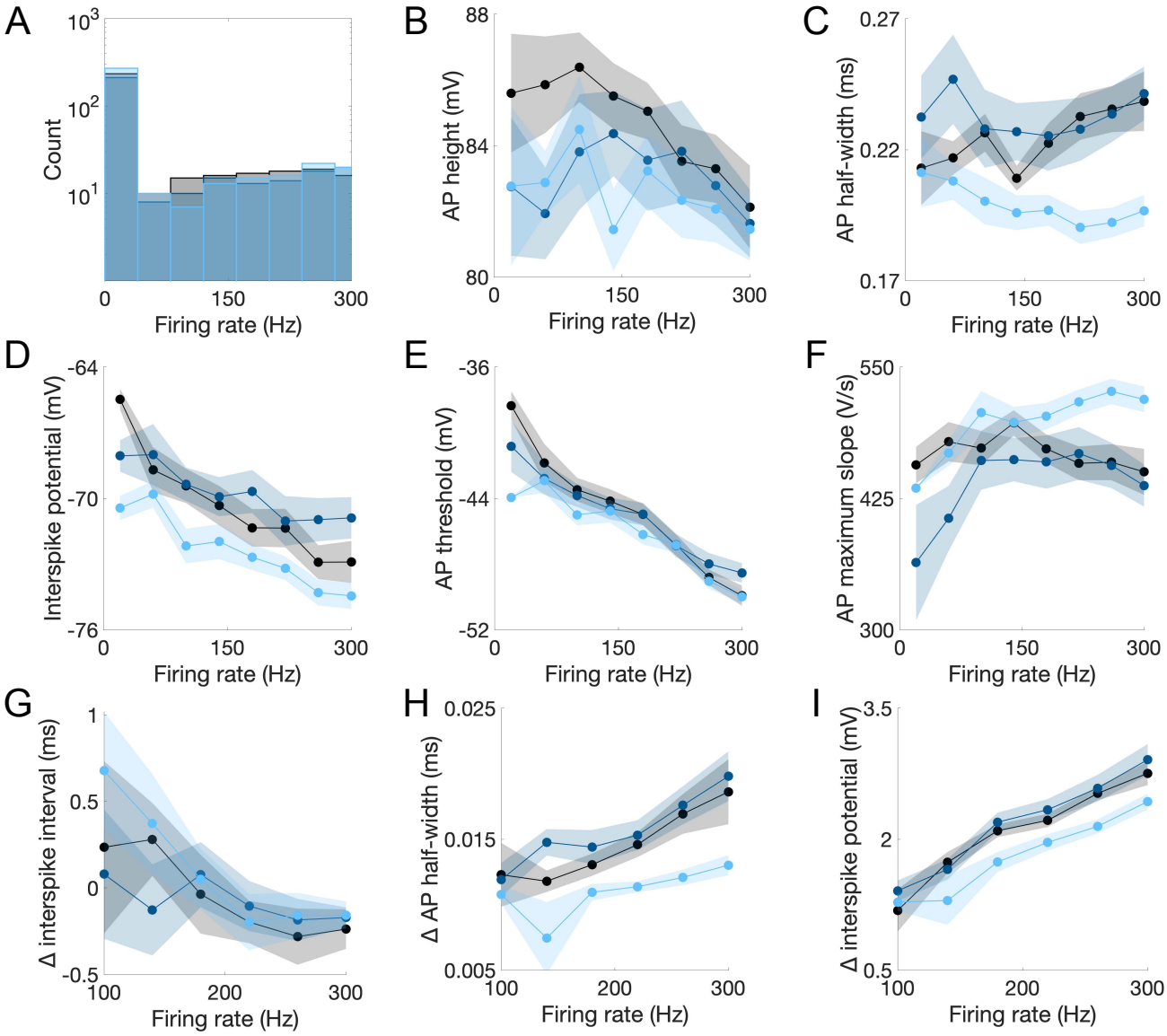
A
Count
Firing rate (Hz)
B
AP height (mV)
Firing rate (Hz)
C
AP half-width (ms)
Firing rate (Hz)
D
Interspike potential (mV)
Firing rate (Hz)
E
AP threshold (mV)
Firing rate (Hz)
F
AP maximum slope (V/s)
Firing rate (Hz)
G
Δ interspike interval (ms)
Firing rate (Hz)
H
Δ AP half-width (ms)
Firing rate (Hz)
I
Δ interspike potential (mV)
Firing rate (Hz)

Fig. S5. Extended analysis of PV intrinsic properties following Kv6.4 deletion.
A, Histogram of firing rate (Hz) distribution (within 300 Hz) for all recordings, independent of current injection, across groups described in **Fig. 3**.
B, AP height (mV) across firing rate for all recordings.
C-F, As in **B** for AP half-width (ms) (**C**), interspike potential (mV) (**D**), AP threshold (mV) (**E**), and AP maximum slope (V/s) (**F**).
G, Change (Δ) in interspike interval (ISI; ms), defined as $ISI_{49-50} – ISI_{2-3}$, across firing rate in recordings containing ≥50 APs.
H-I, As in **G**, for Δ AP half-width (ms), defined as AP_{50} half-width – AP_2 half-width (**H**), and Δ interspike potential (mV), defined as AP_{50} interspike potential – AP_2 interspike potential (**I**).
Mean ± SEM displayed.

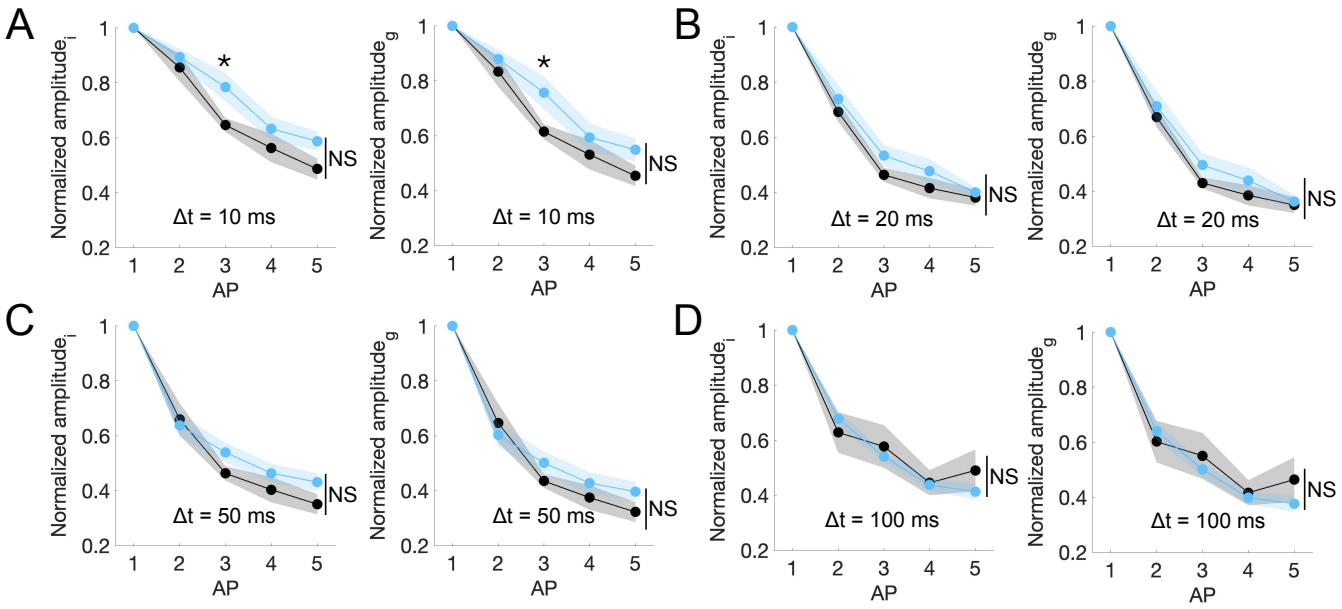
A
B
C
D
Normalized amplitude$_i$
Normalized amplitude$_g$
AP
Δt = 10 ms
Δt = 20 ms
Δt = 50 ms
Δt = 100 ms
NS
*

Fig. S6. Paired pulse depression at PV-PYR synapses across varying interstimulus intervals following Kv6.4 deletion.

A-D, Amplitude of inhibitory current (i; *left*) and conductance (g; *right*) across groups, normalized to response from the first AP, during trains of five presynaptic action potentials, as described in **Fig. 4**. Trains were delivered with an ISI (Δt) of 10 ms (**A**), 20 ms (**B**), 50 ms (**C**), and 100 ms (**D**). Mean ± SEM displayed. * $P < 0.05$; NS: not statistically significant. Unpaired two-tailed t-tests or repeated-measures ANOVA (Greenhouse-Geisser corrected).

Datasets

Dataset S1 (separate file). Raw data and summary data for Fig. 1 and Fig. S1.

Dataset S2 (separate file). Summary data for Fig. 3 and Fig. S4.

Dataset S3 (separate file). Summary data for Fig. 4 and Fig. S6.